REPORT DOCUMENTATION PAGE

Form Approved
OMB No. 0704-0188

1. REPORT DATE *(DD-MM-YYYY)*	2. REPORT TYPE	3. DATES COVERED *(From - To)*
02-06-2011	Journal Article	

4. TITLE AND SUBTITLE
Evaluation and Sensitivity Analysis of an Ocean Model Response to Hurricane Ivan

5a. CONTRACT NUMBER

5b. GRANT NUMBER

5c. PROGRAM ELEMENT NUMBER
0602435N

6. AUTHOR(S)
G. Halliwell, Lynn Shay, J. Brewster, William J. Teague

5d. PROJECT NUMBER

5e. TASK NUMBER

5f. WORK UNIT NUMBER
73-6248-I39-5

7. PERFORMING ORGANIZATION NAME(S) AND ADDRESS(ES)
Naval Research Laboratory
Oceanography Division
Stennis Space Center, MS 39529-5004

8. PERFORMING ORGANIZATION REPORT NUMBER
NRL/JA/7330-09-9213

9. SPONSORING/MONITORING AGENCY NAME(S) AND ADDRESS(ES)
Office of Naval Research
800 N. Quincy St.
Arlington, VA 22217-5660

10. SPONSOR/MONITOR'S ACRONYM(S)
ONR

11. SPONSOR/MONITOR'S REPORT NUMBER(S)

12. DISTRIBUTION/AVAILABILITY STATEMENT
Approved for public release, distribution is unlimited.

13. SUPPLEMENTARY NOTES

20110804237

14. ABSTRACT

An ocean model response to Hurricane Ivan (2004) over the northwest Caribbean Sea and Gulf of Mexico is evaluated to guide strategies for improving performance during strong forcing events in a region with energetic ocean features with the ultimate goal of improving coupled tropical cyclone forecasts. Based on prior experience, a control experiment is performed using quasi-optimal choices of initial ocean fields, atmospheric forcing fields, air -sea flux parameterizations, vertical mixing parameterizations, and both horizontal and vertical resolutions. Alternate experiments are conducted by altering one single model attribute and comparing the results to SST analyses and moored ADCP current measurements to quantify the sensitivity to that attribute and identify where to concentrate model improvement efforts. Atmospheric forcing that does not resolve the eye and eyewall of the storm (scales >10 km) substantially degrades the ocean response. Ordering other model attributes from greatest to least sensitivity, ocean model initialization with regard to the accuracy of upper-ocean temperature -salinity profiles along with accurate location of ocean currents and eddies is the most important factor for ensuring good ocean model performance. Ocean dynamics ranks second in this energetic ocean region because a one-dimensional ocean model fails to capture important physical processes that affect SST cooling. Wind stress drag coefficient parameterizations that yield values exceeding 2.5×10^{-3} at high wind speeds or that remain $<2.0 \times 10^{-3}$ over all wind speeds reduce the realism of wind-driven current profiles and have a large impact on both SST cooling and the heat flux from ocean to atmosphere. Turbulent heat flux drag coefficient parameterizations substantially impact the surface heat flux while having little impact on SST cooling, which is primarily controlled by entrainment at the mixed layer base. Vertical mixing parameterizations have a moderate impact on SST cooling but a comparatively larger impact on surface heat flux. The impacts of altering the horizontal and vertical resolutions are small, with horizontal resolution of ≈10 km and vertical resolution of ≈10 m in the mixed layer being adequate. Optimal choices of all attributes for simulating the ocean response to Ivan are identified.

15. SUBJECT TERMS
hurricanes, ocean models, sensitivity studies, sea surface temperature

16. SECURITY CLASSIFICATION OF:			17. LIMITATION OF ABSTRACT	18. NUMBER OF PAGES	19a. NAME OF RESPONSIBLE PERSON
a. REPORT	b. ABSTRACT	c. THIS PAGE			William J. Teague
Unclassified	Unclassified	Unclassified	UL	25	19b. TELEPHONE NUMBER *(Include area code)* 228-688-4734

Evaluation and Sensitivity Analysis of an Ocean Model Response to Hurricane Ivan

G. R. HALLIWELL JR.,* L. K. SHAY, AND J. K. BREWSTER

MPO/RSMAS, University of Miami, Miami, Florida

W. J. TEAGUE

Naval Research Laboratory, Stennis Space Center, Mississippi

(Manuscript received 19 June 2009, in final form 11 December 2009)

ABSTRACT

An ocean model response to Hurricane Ivan (2004) over the northwest Caribbean Sea and Gulf of Mexico is evaluated to guide strategies for improving performance during strong forcing events in a region with energetic ocean features with the ultimate goal of improving coupled tropical cyclone forecasts. Based on prior experience, a control experiment is performed using quasi-optimal choices of initial ocean fields, atmospheric forcing fields, air–sea flux parameterizations, vertical mixing parameterizations, and both horizontal and vertical resolutions. Alternate experiments are conducted by altering one single model attribute and comparing the results to SST analyses and moored ADCP current measurements to quantify the sensitivity to that attribute and identify where to concentrate model improvement efforts. Atmospheric forcing that does not resolve the eye and eyewall of the storm (scales >10 km) substantially degrades the ocean response. Ordering other model attributes from greatest to least sensitivity, ocean model initialization with regard to the accuracy of upper-ocean temperature–salinity profiles along with accurate location of ocean currents and eddies is the most important factor for ensuring good ocean model performance. Ocean dynamics ranks second in this energetic ocean region because a one-dimensional ocean model fails to capture important physical processes that affect SST cooling. Wind stress drag coefficient parameterizations that yield values exceeding 2.5×10^{-3} at high wind speeds or that remain $<2.0 \times 10^{-3}$ over all wind speeds reduce the realism of wind-driven current profiles and have a large impact on both SST cooling and the heat flux from ocean to atmosphere. Turbulent heat flux drag coefficient parameterizations substantially impact the surface heat flux while having little impact on SST cooling, which is primarily controlled by entrainment at the mixed layer base. Vertical mixing parameterizations have a moderate impact on SST cooling but a comparatively larger impact on surface heat flux. The impacts of altering the horizontal and vertical resolutions are small, with horizontal resolution of ~10 km and vertical resolution of ~10 m in the mixed layer being adequate. Optimal choices of all attributes for simulating the ocean response to Ivan are identified.

1. Introduction

Coupled ocean–atmosphere general circulation models have become increasingly important for tropical cyclone (TC) forecast guidance at operational prediction centers. Implementation and advancement of coupled TC forecast models such as the Geophysical Fluid Dynamics Laboratory (GFDL) model and more recently the Hurricane Weather Research and Forecast (HWRF) model have significantly improved track forecasts by the National Hurricane Center (e.g., Bender et al. 2007). However, little improvement has been realized for intensity forecasts. Given that the ocean provides the thermal energy for intensification, errors and biases in the ocean component of coupled TC forecast models may contribute to the low skill of intensity forecasts.

When atmospheric conditions are favorable, TC intensification often occurs as a storm passes over regions with high upper-ocean heat content. This is particularly true for potentially dangerous rapid intensification. The impacts of the Loop Current (LC) and warm-core anticyclones in the Gulf of Mexico (GOM) are documented for Hurricanes Gilbert (1988) and Opal (1995) (Jacob

* Current affiliation: NOAA/AOML/Physical Oceanography Division, Miami, Florida.

Corresponding author address: George Halliwell, NOAA/AOML/PhOD, 4301 Rickenbacker Cswy., Miami, FL 33149.
E-mail: george.halliwell@noaa.gov

DOI: 10.1175/2010MWR3104.1

et al. 2000; Hong et al. 2000; Shay et al. 2000; Jacob and Shay 2003), and also for Hurricanes Katrina and Rita (2005) (Scharroo et al. 2005; Sun et al. 2006, Shay 2009; Jaimes and Shay 2009, 2010). Similar results have been obtained in the western Pacific for Typhoon Maemi (2003) (Lin et al. 2005) and have also been obtained in statistical studies of multiple storms (Wada and Usui 2007; Lin et al. 2008). Numerical models have reproduced the positive impacts of high heat content on intensification (Schade and Emanuel 1999; Bender and Ginis 2000; Hong et al. 2000; Emanuel et al. 2004; Lin et al. 2005; L. Wu et al. 2005; C.-C. Wu et al. 2007). Low ocean heat content can inhibit intensification, possibly contributing to the weakening of both Ivan (Walker et al. 2005) and Rita (Sun et al. 2006; Shay and Uhlhorn 2008; Jaimes and Shay 2009, 2010) as they passed over cold-core cyclones in the GOM.

To correctly forecast intensity evolution, the ocean component of coupled forecast models must accurately predict the rate and pattern of SST cooling relative to the eye of the hurricane. However, ocean models have not been thoroughly evaluated for this purpose. The present study evaluates an ocean model response to Hurricane Ivan (2004) over the northwest Caribbean Sea and GOM. Evaluation is difficult because ocean general circulation models incorporate a large suite of numerical algorithms and subgrid-scale parameterizations of processes not explicitly resolved by the model grid. Surface fluxes of momentum, heat, and mass (evaporation) must also be parameterized. The ocean state must be accurately initialized, while the impacts of the ocean outside the model domain must be provided with specified open-ocean boundary conditions. Model performance may also be affected by the horizontal and vertical resolutions of the grid. The relative impacts of these attributes on predicting the SST response are poorly known, and it is not clear where the greatest effort toward improving model performance should be targeted. Model improvement will be difficult because errors and biases in ocean simulations arise simultaneously from all of these factors. For example, modifications of the vertical mixing parameterization that improve the upper-ocean response may actually be compensating for errors and biases resulting from surface flux parameterizations. A credible model improvement effort will require a thorough understanding of how model numerics and parameterizations impact the predicted upper-ocean response to TC forcing.

The overarching goal of this analysis is to determine how to best invest our collective efforts toward improving ocean model performance. Within this context, sensitivity to eight individual model attributes is examined: 1) horizontal resolution, 2) vertical resolution, 3) vertical mixing and viscosity parameterizations, 4) wind stress drag coefficient parameterization, 5) turbulent heat flux drag coefficient parameterization, 6) atmospheric forcing resolution, 7) ocean model initialization, and 8) ocean dynamics (three- versus one-dimensional). Multiple experiments are performed, with one identified as the control experiment and the others identical to it except for altering one single attribute. Sensitivity to each attribute is quantified and their relative levels of importance are ranked without the complicating influence of atmospheric feedbacks that would be present when using a coupled model. Analysis is performed on three fields based on their expected level of importance regarding storm intensity. In addition to the obvious choice of SST, ocean–atmosphere turbulent heat flux (latent plus sensible) averaged within specified radii of the storm center along with upper-ocean velocity profiles are considered. Heat flux is directly associated with impacts of the ocean on intensity while accurate representation of velocity profiles is necessary for the model to reproduce the shear-driven turbulence at the ocean mixed layer (OML) base that is primarily responsible for SST cooling.

In addition to this sensitivity analysis, we assess the overall realism of the simulated ocean response to Hurricane Ivan within the limits of available observations, specifically an SST analysis generated from satellite and in situ observations and velocity profiles obtained from moored acoustic Doppler current profiler (ADCP) measurements. Unfortunately, targeted aircraft observations that could have provided simultaneous subsurface profiles of temperature, salinity, and currents before, during, and after Ivan were not available, thus limiting the extent of the evaluation that could be performed.

Section 2 describes the ocean model, forcing fields, and observations. Section 3 summarizes the model experiments and analysis procedures. The evaluation and sensitivity analysis are presented in the next three sections, with section 4 focusing on the SST response pattern, section 5 emphasizing thermal fluxes from the ocean to the atmosphere during Ivan, and section 6 addressing the ocean dynamics, specifically wind-driven upwelling and forced upper-ocean velocity fluctuations that are important for shear-driven OML entrainment. Concluding remarks are presented in section 7.

2. Model and observations

a. HYCOM

The Hybrid Coordinate Ocean Model (HYCOM) is a primitive equation ocean model that uses a hybrid vertical coordinate designed to quasi-optimally resolve vertical structure throughout the ocean. This coordinate system is isopycnic in the stratified ocean interior, but dynamically transitions to level coordinates near the surface to provide resolution in the surface mixed layer and to either level or

terrain-following (σ) coordinates in the coastal ocean. This strategy enables HYCOM to use advanced turbulence closures for vertical mixing and also to be used as both a coastal and open-ocean model while retaining the advantages of isopycnic coordinates in the stratified ocean interior. Model equations and an initial evaluation of the hybrid vertical grid generator are presented in Bleck (2002). Subsequent evolutions and further evaluations of the model are summarized in Chassignet et al. (2003, 2007) and Halliwell (2004).

b. Model initialization

All experiments except one are initialized with fields provided by a data-assimilative hindcast that employs the Navy Coupled Ocean Data Assimilation (NCODA) optimum interpolation system (Cummings 2005) to assimilate satellite altimetry and SST along with in situ observations. Altimetry assimilation ensures that major ocean features such as the LC and associated warm-core anticyclones and cold-core cyclones are initialized in their correct locations. This is especially important in the GOM and Caribbean Sea due to the limited availability of in situ observations. The NCODA system uses the Cooper and Haines (1996) algorithm to provide a downward projection of anomalous temperature and salinity profiles associated with anomalous sea surface heights (SSHs). Halliwell et al. (2008) evaluated the same GOM NCODA hindcast product regarding ocean model initialization for several storms including Ivan, noting a consistent cold bias that was not as severe before Ivan as before other storms.

To assess the sensitivity to initialization, one experiment is initialized from a nonassimilative GOM simulation where the ocean features are unconstrained by observations. Significant differences exist in the LC path and in the locations of warm-core anticyclones and cold-core cyclones between the two initialization products (Fig. 1). The two cold-core cyclones present in the data-assimilative initialization (Fig. 1, red arrows) that are critically important for simulating the SST response pattern forced by Ivan (Halliwell et al. 2008) are not present at the same locations in the non-assimilative initialization. For all experiments, the outer model product used for initialization also provides the required open-ocean boundary conditions during the runs.

c. Surface atmospheric forcing

Realistic atmospheric forcing fields that resolve the inner-core structure of hurricanes are required to perform meaningful ocean model evaluation. Atmospheric or coupled ocean–atmosphere models run globally by major operational centers presently have horizontal resolutions that are far too coarse. The most realistic available choice is the Coupled Ocean–Atmosphere Mesoscale Prediction System (COAMPS; Hodur 1997) with fields available at 27-km resolution. Since even this resolution is too coarse, we use the objectively analyzed 10-m vector wind fields (H*WIND; Powell et al. 1998), from the National Oceanic and Atmospheric Administration/Atlantic Oceanographic and Meteorological Laboratory/Hurricane Research Division (NOAA/AOML/HRD), to improve the inner-core structure. Briefly, these fields are produced by the objective analysis of aircraft observations combined with other available meteorological observations. The H*WIND fields accurately represent both the maximum wind speed and the radius of maximum wind speed (R_{MAX}), the latter being approximately 45 km for Ivan. The low resolution of the COAMPS product results in an R_{MAX} that is about twice as large as observed and a maximum wind that is reduced by 40%–50%.

Ideally, higher-resolution atmospheric forcing fields from a fine-resolution coupled model such as HWRF should be used. However, no such product presently exists for Ivan where the storm both follows the correct path and maintains the correct intensity with sufficient accuracy at all times. This is especially true for studying the upper-ocean velocity response for reasons described in section 2d.

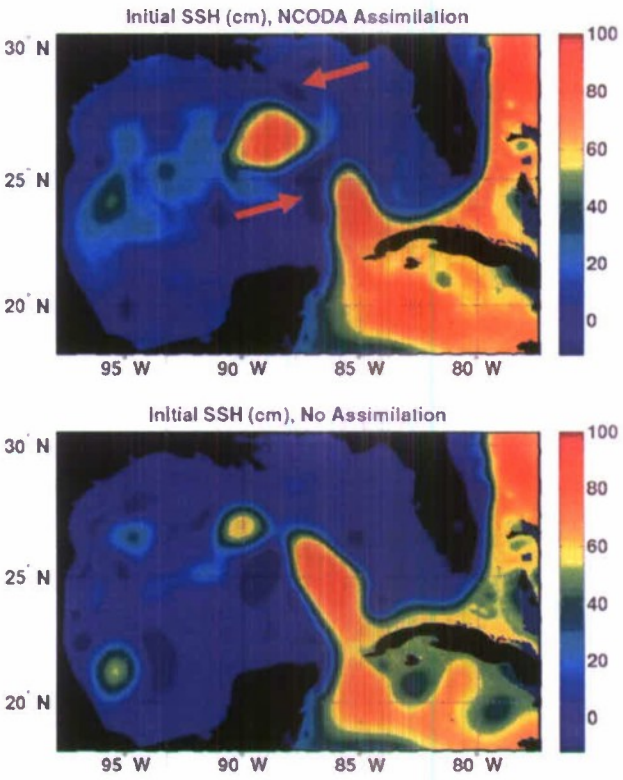

FIG. 1. SSH maps at 0000 UTC 10 Sep 2004 from initial model fields provided by (top) a data-assimilative GOM hindcast for experiments GOM1–GOM13 plus GOM15 and (bottom) a non-assimilative GOM simulation for experiment GOM14. The red arrows point to the two cold-core cyclones where Ivan forced large cooling.

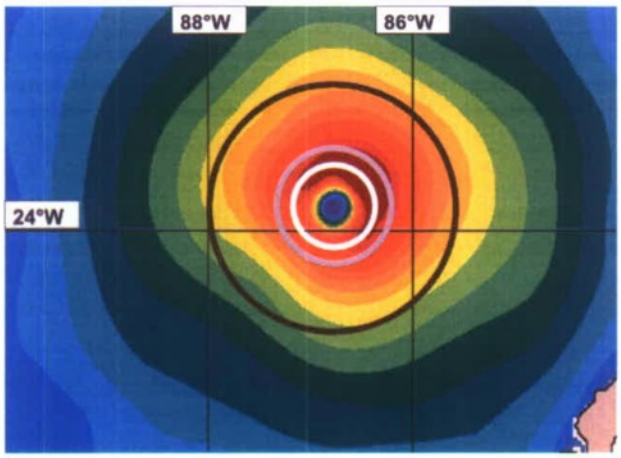

FIG. 2. Map of 10-m wind speed in the eastern GOM on 15 Sep from the blended COAMPS–H*WIND forcing product. The white circle illustrates the radius of maximum wind R_{MAX} = 45 km. The magenta ($1.4R_{MAX}$) and black ($3.0R_{MAX}$) circles illustrate the averaging domains for the air–sea thermal heat flux sensitivity analysis in Fig. 9.

Wind stress and wind speed forcing fields are generated following the procedure described in Halliwell et al. (2008) that blends vector wind maps from H*WIND with output from the 1° Navy Operational Global Atmospheric Prediction System (NOGAPS) atmospheric model. Improved fields are generated for the present study because the H*WIND fields are blended with the higher-resolution COAMPS atmospheric model and because the H*WIND fields are now available at higher temporal resolution (3-hourly versus only at the time of research aircraft flights). The 3-hourly COAMPS and H*WIND wind component fields were temporally interpolated to 30-min intervals and then blended using Eqs. (5) and (6) in Halliwell et al. (2008) with r_1 = 160 km and r_2 = 420 km. Thus, the vector wind fields are 100% (0%) H*WIND < 160 km (>420 km) from the storm center. One realization of the blended wind speed forcing is presented in Fig. 2. Vector wind stress fields are calculated from bulk formulas using a prescribed drag coefficient C_D.

Other required forcing fields (air temperature, specific humidity, net radiative heat fluxes, and precipitation) are provided entirely by the COAMPS model. These fields are horizontally interpolated onto the ocean model grid points and then temporally interpolated to 30-min intervals. Surface turbulent (latent plus sensible) heat fluxes are calculated during model experiments using bulk formulas. After Ivan makes landfall, the wind speed and wind stress forcing revert to the 3-hourly COAMPS fields.

d. Observations

Cooling patterns are evaluated against daily SST fields generated by the objective analysis of in situ observations along with Advanced Very High Resolution Radiometer (AVHRR) and microwave satellite observations onto a 0.25° global grid (Reynolds et al. 2007), hereinafter referred to as the "blended" SST. Simulated upper-ocean velocity profiles are evaluated against moored velocity measurements. Hurricane Ivan passed directly over an array of moored ADCPs deployed by the Naval Research Laboratory over the continental shelf and slope south of Mobile, Alabama, as part of the Slope to Shelf Energetics and Exchange Dynamics (SEED) project (Carnes et al. 2008; Teague et al. 2006). Six shallow ADCP moorings were deployed; three each near the 60- and 90-m isobaths. Eight other ADCP moorings were deployed over the continental slope, four along the 500-m isobath and four along the 1000-m isobath near De Soto Canyon. Teague et al. (2007) used this dataset to study fundamental properties of the ocean response to Ivan over this shelf-slope region, which represents a challenge for ocean models (e.g., transition between open-ocean and coastal regimes).

Herein, we evaluate the simulated velocity response to Ivan at four of the ADCP moorings at differing locations relative to the eye with different bottom depths (see inset, Fig. 5). Moorings 7 and 9 are located over the continental slope of the northern GOM near 500-m depth and were located under the western and eastern parts of the eyewall, respectively. Moorings 1 and 3 are located over the middle continental shelf near 50-m depth and were also located under the western and eastern parts of the eyewall, respectively. The forced velocity response differs markedly over small differences relative to the eye due to differences in wind vector rotation on opposite sides of the eye. This analysis therefore requires that the storm in the atmospheric forcing fields follow the true path with high accuracy (<10-km lateral error). No available product other than H*WIND provides this accuracy to the best of our knowledge.

3. Numerical experimentation

Fifteen non-assimilative HYCOM simulations were conducted to assess model sensitivity to eight attributes (Table 1). All experiments were conducted within a domain spanning the GOM and northwest Caribbean Sea, henceforth referred to as the GOM domain, that is situated on a Mercator grid with 0.04 × 0.04 cosφ degree resolution (≈4 km), where φ is latitude. The coastline follows the actual land–sea boundary but a minimum water depth of 2 m is enforced. Freshwater input from 12 rivers is included.

All experiments are referenced to a control experiment (GOM1) that has the attributes listed in the middle column of Table 1. The NCODA GOM hindcast within which it is nested was conducted with 20 vertical layers

TABLE 1. Summary of the model simulations. The first column lists the model attributes while the second column lists the specific attributes of the control experiment GOM1. The third column lists all of the alternate experiments along with the new attribute.

Model attribute	Control expt (GOM1)	Alternate expts
Horizontal resolution	0.04° Mercator	GOM2: 0.08° Mercator
Vertical resolution	26 layers, 4–8 m in OML	GOM3: 21 layers, 7.5–15 m in OML GOM4: 31 layers, 3–5 m in OML
Vertical mixing	KPP	GOM5: MY GOM6: GISS
C_D	Donelan	GOM7: Powell GOM8: Large and Pond GOM9: Large and Pond (capped) GOM10: Shay and Jacob GOM11: Jarosz et al.
C_{EL}, C_{ES}	COARE 3.0 algorithm	GOM12: Kara et al.
Atmospheric forcing	27-km COAMPS + H*WIND	GOM13: 27-km COAMPS only
Outer model	NCODA GOM hindcast	GOM14: free GOM simulation
Ocean dynamics	Three-dimensional	GOM15: one-dimensional

on the identical 0.04° mesh. The control experiment has 26 layers, with additional layers added to provide vertical resolution of 4–8 m in the OML (Fig. 3, middle panel). The six new layers are assigned isopycnic target densities lighter than any water present within the GOM domain to force them to remain in the constant-thickness layers at the top of the water column. Vertical mixing is provided by the *K*-profile parameterization (KPP) of Large et al. (1994) that has been modified in HYCOM to include a bottom boundary layer parameterization (Halliwell et al. 2009). The vector wind stress forcing field is calculated prior to the model run using the C_D representation of Donelan et al. (2004). The surface turbulent heat flux and evaporation rate are calculated during the model run using the default parameterization of the latent and sensible heat flux drag coefficients C_{EL} and C_{ES}, specifically version 3.0 of the Coupled Ocean–Atmosphere Response Experiment (COARE 3.0) algorithm (Fairall et al. 1996; Andreas and DeCosmo 2002). Model fields are initialized on 0000 UTC 10 September 2004 and the simulation is run for 3 weeks.

The remaining experiments (GOM2–GOM15) each differ from GOM1 by altering a single model attribute as listed in Table 1 to examine the sensitivity of the ocean response. The alternate horizontal resolution experiment GOM2 is run in the same domain, but on a 0.08° Mercator mesh consisting of every other point of the high-resolution grid. Two alternate vertical resolutions are tested, one coarser (21 layers, GOM3) and one finer (31 layers, GOM4) than the control experiment (Fig. 3; Table 1), requiring 1 and 11 additional layers, respectively, to be added to the outer model fields. Two alternate vertical mixing parameterizations are evaluated: the Mellor–Yamada (MY) level 2.5 turbulence closure (Mellor and Yamada 1982) in GOM5 and the Goddard Institute for Space Studies (GISS) level 2 turbulence closure (Canuto et al. 2001, 2002) in GOM6. For the wind stress drag coefficient, experiments GOM7–GOM11 use the algorithms of: Powell et al. (2003), Large and Pond (1981), Large and Pond with C_D capped at a constant value above 30 m s^{-1}, Shay and Jacob (2006), and Jarosz et al. (2007). These parameterizations are graphed in Fig. 4. One alternate representation of C_{EL} and C_{ES} that is built into HYCOM is used in GOM12, specifically the Kara et al. (2002) algorithm. Coefficients from both algorithms are graphed in Fig. 4 for a representative choice of air temperature and SST. Experiment GOM13 evaluates the sensitivity to atmospheric forcing resolution by using COAMPS forcing alone and demonstrates the necessity of using blended H*WIND forcing for the control experiment. GOM14 is nested in the non-assimilative outer model to evaluate sensitivity to initialization. Finally, GOM15 uses the HYCOM code configured as one-dimensional ocean models run independently at each grid point to demonstrate the impacts of three-dimensional ocean dynamics.

4. SST cooling

a. Results from the control experiment

The control simulation is conducted with the same model parameterizations as the experiment analyzed by Halliwell et al. (2008) to document the impacts of ocean model initialization. However, improved comparison between model and observations is expected in the present analysis because of 1) the use of improved blended forcing, 2) upgrades to the model code, and 3) the use of a more optimal SST analysis for model evaluation. As in the earlier study, poststorm SST cooling in the control experiment is largest within the two cold-core cyclones initially present in the eastern GOM (Figs. 1 and 5). The comparison of model results to an SST analysis derived solely from microwave satellite measurements performed by Halliwell et al. (2008) demonstrated that the model caused a substantial overcooling in both cyclones. However, a visual comparison of the post-Ivan AVHRR images analyzed by Walker et al. (2005) to the post-Ivan microwave SST fields presented in Halliwell et al. (2008) suggested that the daily microwave SST analysis may have underestimated the actual cooling that occurred within

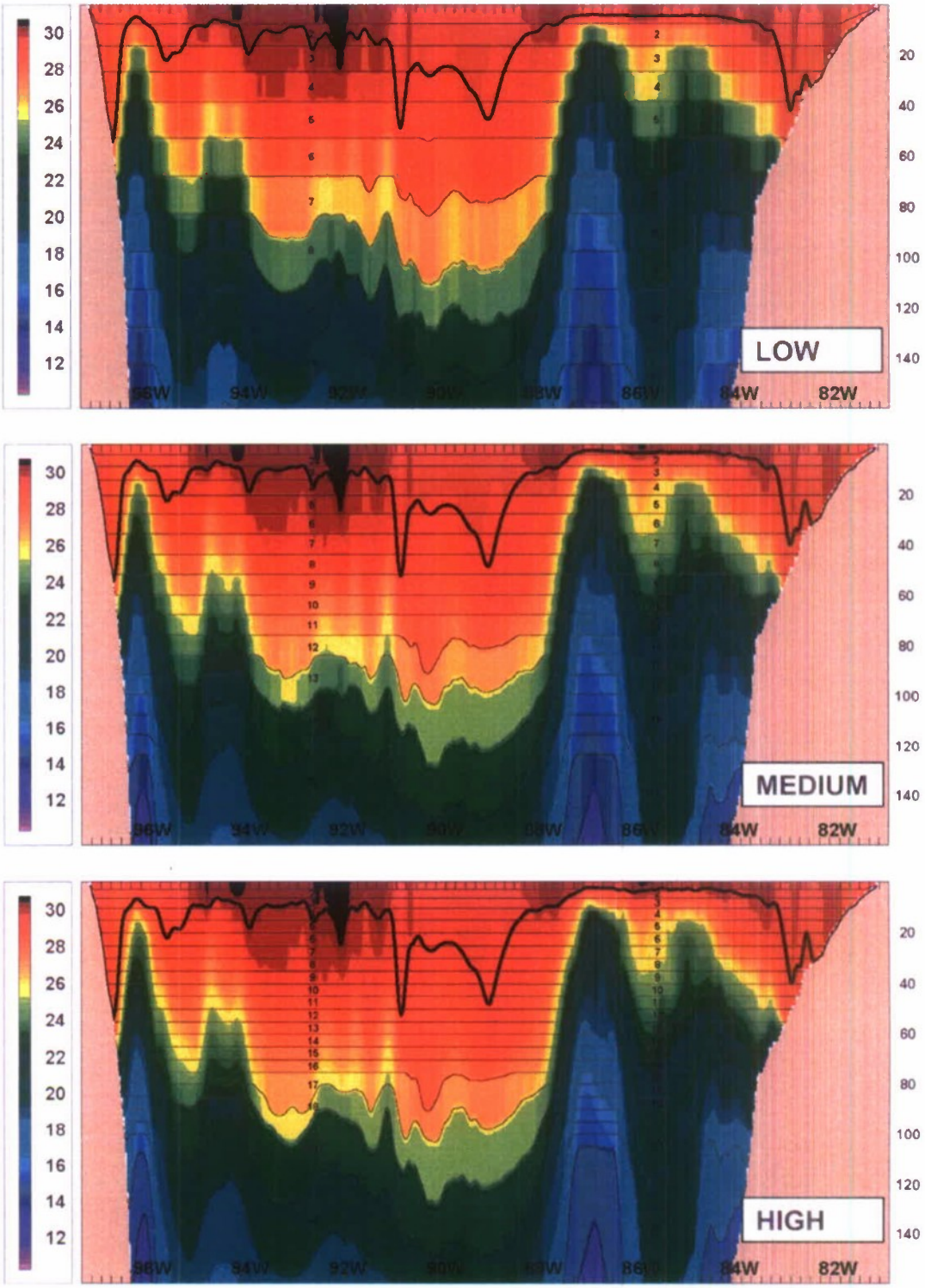

FIG. 3. Upper-ocean zonal cross sections of initial (0000 UTC 10 Sep 2004) ocean temperature fields provided by the data-assimilative GOM hindcast for the three different vertical resolutions tested: (top) low resolution used for GOM3, (bottom) high resolution used for GOM4, and (middle) medium resolution used for all other experiments. The fixed coordinates near the surface follow the HYCOM convention of increasing in thickness with depth until a prescribed maximum thickness is reached. The range of layer thicknesses for each experiment is listed in Table 1.

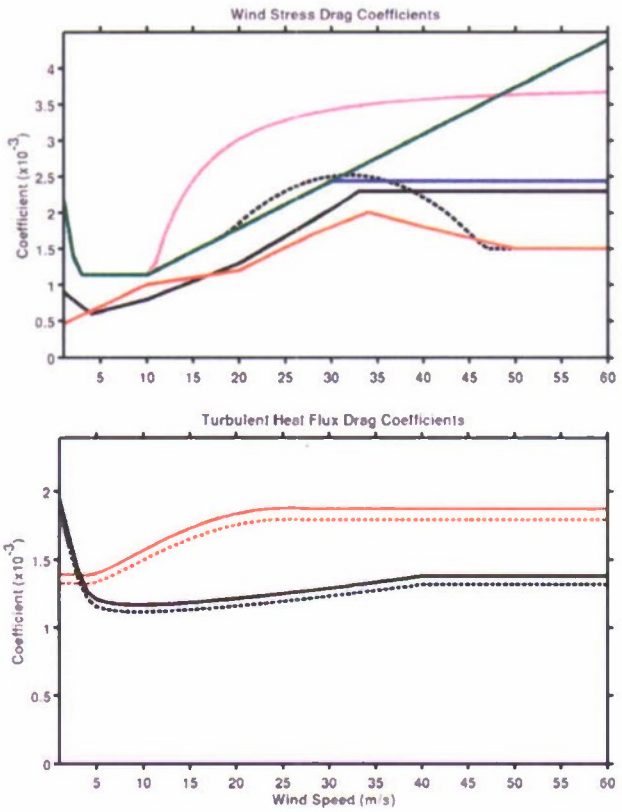

FIG. 4. (top) The wind stress drag coefficients C_D as a function of wind speed and (bottom) the latent and sensible heat flux coefficients C_{EL} and C_{ES} as a function of wind speed provided to model experiments. The six wind stress drag coefficients are Donelan (black); Powell (red); Large and Pond (green); Large and Pond capped (blue above 30 m s^{-1}); Shay and Jacob (magenta), which reverts to Large and Pond below 10 m s^{-1}; and Jarosz et al. (black dashed), which reverts to Large and Pond below 20 m s^{-1} and levels off at 1.5×10^{-3} above 47 m s^{-1}. The heat flux coefficients are the COARE 3.0 algorithm (C_{EL}, black solid; C_{ES}, black dashed) and Kara et al. (C_{EL}, red solid; C_{ES}, red dashed), and are calculated assuming an air temperature of 27°C and an SST of 29°C. Similar differences between these two algorithms are realized for different choices of air temperature and SST.

these cyclones. The daily, 0.25° Reynolds et al. (2007) blended analysis of microwave, AVHRR, and in situ SST was selected for the present study because it produced a post-Ivan SST that was colder by ≈2°C in the northern cyclone and ≈1°C in the southern cyclone, more in agreement with the AVHRR images. With this change, the control experiment overcooled with respect to the SST analysis by only 0.6° in the northern cyclone (Table 2). However, it still excessively overcooled by 4.3°C in the southern cyclone. Because the simulated cooling over the remainder of the eastern GOM and northwest Caribbean Sea is generally close to the observed magnitude (Fig. 5), large errors were generally confined to the southern cyclone.

The impacts of ocean features on the cooling pattern are explored further by graphing temperature as a function of time and depth at the two locations illustrated in Fig. 5 (top): one located at the eastern edge of the detached warm anticyclone and the other located near the center of the southern cold-core cyclone. Both points are located about 45 km, or one radius of maximum wind speed (R_{MAX}), east of the track with R_{MAX} estimated from the blended wind speed forcing field (Fig. 2). This is the approximate location relative to the track where the largest near-inertial currents are forced (e.g., Price 1981; Sanford et al. 2007). These profiles are calculated during model runs by inserting synthetic moorings at these two locations with instruments deployed at 5-m vertical intervals. Model fields are sampled at each synthetic instrument using two-dimensional polynomial horizontal interpolation to the mooring locations and then performing linear vertical interpolation to instrument depths.

SST cooling is larger within the cyclone (10°C) compared to the anticyclone (3°C) because of both the thinner initial surface warm layer and the stronger wind-driven upwelling (Fig. 6). To highlight the contribution of upwelling, the terms of the OML thickness balance are estimated:

$$w_E = w_M - \frac{\partial z_M}{\partial t}, \tag{1}$$

where w_E is the entrainment velocity and w_M is the vertical velocity at the depth of the OML base z_M. The two terms on the right side are diagnosed from the model output, and then w_E is estimated as a residual. The OML base is diagnosed as the depth where the temperature is 0.5°C colder than the surface (layer 1) temperature. Vertical velocity is diagnosed during model runs at the central depth of each model layer at each grid point following Halliwell et al. (2003). It is then horizontally interpolated to the synthetic mooring locations using two-dimensional polynomial interpolation and then vertically interpolated to the OML base using linear interpolation.

These three terms reveal large differences in the OML depth balance between the warm ring and cold cyclone (Fig. 6). Prior to the time the eye passes the warm-ring location, w_M is small so that $w_E \approx -\partial z_M/\partial t$, indicating that upwelling makes little contribution to the cooling. After Ivan passes, OML penetration abruptly ceases as w_M gradually increases, peaking about 0.2 inertial periods (IPs) or about 5 h after passage and then remaining positive through 0.4 IP. During this time interval, w_E is small or negative (detrainment) and upwelling still has little impact on cooling. By comparison, upwelling in the cold cyclone makes a substantial contribution to cooling both prior to and during storm passage, with w_E peaking at the time of passage and remaining positive for about 0.25 IP

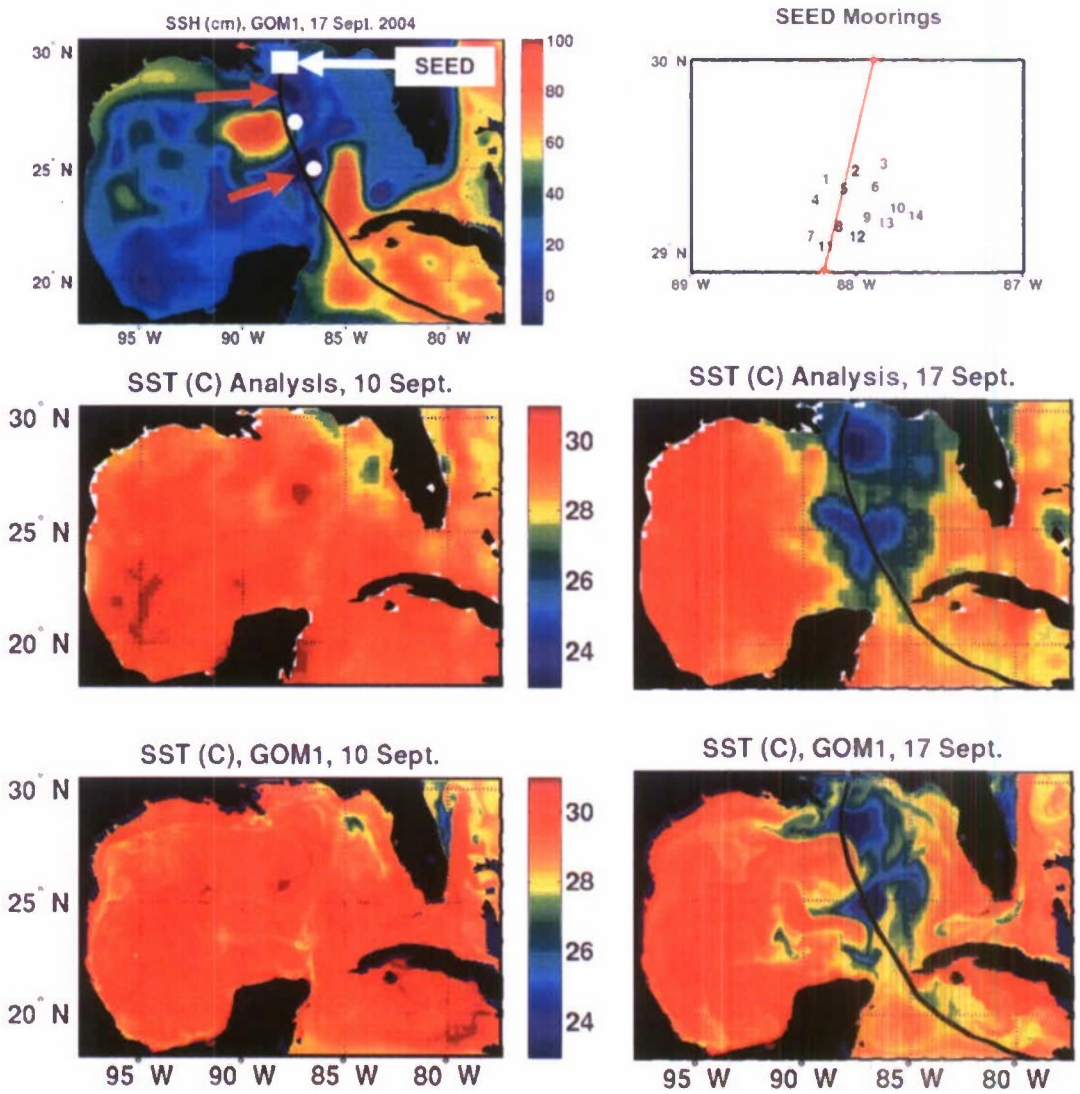

FIG. 5. Map of (top left) SSH on 17 Sep 2004 shortly after Ivan made landfall (track in black line), illustrating the locations of the LC, the detached warm ring, and the two cyclonic eddies (red arrows) near the time of maximum cooling in the eastern GOM. A white rectangle marks the location of a SEED mooring (Teague et al. 2007) and (top right) the inset at right illustrates mooring locations with the approximate track of Ivan shown by the red line. The other two unmarked white dots in the SSH map represent the locations sampled by synthetic instruments and described in Fig. 6. The remaining panels present SST maps for (left) 10 and (right) 17 Sep 2004 for (top) the Reynolds et al. (2007) blended analysis of in situ observations plus infrared and microwave satellite data and (bottom) from the control experiment GOM1.

thereafter. The rate of OML deepening is small for about 0.2 IP prior to passage so that $w_E \approx w_M$. During this time interval, upwelling increases cooling by lifting colder water toward the OML base and by maintaining a thinner OML, with the latter impact resulting in increased OML entrainment by both wind- and buoyancy-forced TKEs at the surface and by shear instability of the wind-driven horizontal flow at the OML base. A thin OML also has relative small thermal inertia and will cool more rapidly for a given entrainment heat flux. Following hurricane passage, entrainment rapidly weakens and the upwelling primarily acts to raise the OML base. Beginning around 0.2 IP after passage when w_M is small, the weak stratification remaining at the OML base permits rapid OML deepening due to large entrainment driven by the shear of the near-inertial current fluctuations. Entrainment cooling remains significant until 0.5 IP after passage and maximum cooling is realized about 0.4 IP (10 h) after Ivan's passage.

Further insights on the impacts of upwelling and other aspects of three-dimensional ocean dynamics are obtained by comparing the evolution of the temperature and vertical velocity profiles from the one-dimensional

TABLE 2. Post-Ivan SST (°C) on 17 Sep 2004 within the northern and southern cold-core cyclones where the largest cooling occurred from both the observations and the 15 experiments along with SST differences between each experiment and the observations. SST values were calculated by averaging over 1° × 1° boxes centered at 28.4°N, 87.4°W (northern cyclone) and 25.0°N, 86.8°W (southern cyclone).

	Northern cold-core cyclone			Southern cold-core cyclone		
Source	SST (°C)	Diff from GOM1	Diff from obs	SST (°C)	Diff from GOM1	Diff from obs
Obs	22.3			23.9		
GOM1	21.7		−0.6	19.6		−4.3
GOM2	21.6	−0.1	−0.7	19.5	−0.1	−4.4
GOM3	21.8	+0.1	−0.5	19.3	−0.3	−4.6
GOM4	21.6	−0.1	−0.7	20.1	+0.5	−3.8
GOM5	22.3	+0.6	0.0	21.4	+1.8	−2.5
GOM6	22.5	+0.8	+0.2	20.2	+0.6	−3.7
GOM7	22.6	+0.9	+0.3	20.5	+0.9	−3.4
GOM8	20.7	−1.0	−1.6	19.0	−0.6	−4.9
GOM9	21.5	−0.2	−0.8	19.2	−0.4	−4.7
GOM10	20.2	−1.5	−2.1	18.1	−1.5	−5.8
GOM11	22.3	+0.6	0.0	19.8	+0.2	−4.1
GOM12	21.7	0.0	−0.6	19.7	+0.1	−4.2
GOM13	23.7	+2.0	+1.4	22.0	+2.4	−1.9
GOM14	23.4	+1.7	+1.1	26.5	+6.9	+2.6
GOM15	22.7	+1.0	+0.4	22.8	+3.2	−1.1

experiment GOM15 to those from the control experiment at the same two locations (Fig. 6). In the absence of wind-driven vertical velocity in both the anticyclone and cyclone, w_E is large prior to and during passage, but then decreases rapidly within 0.1 IP after passage as wind forcing relaxes and the OML approaches its maximum thickness. SST cooling produced by GOM15 is smaller compared to the control, 2° versus 3°C in the anticyclone and 5° versus 10°C in the cyclone (Fig. 6). As discussed earlier, wind-driven vertical velocity is a major contributor to increased cooling in the cyclone. The story is different in the anticyclone because the warm layer that is present 0.5 IP before the storm in GOM15 is thicker than in the control experiment, a situation that likely contributed substantially to the reduced cooling. The different warm layer thicknesses occur because the measurement point is located at the eastern edge of the anticyclone and the warm layer there becomes thinner over the first few days of the simulation as this feature propagates westward. This analysis demonstrates the critical importance of ocean dynamics not only because wind-driven upwelling can contribute significantly to SST cooling, but also because the upwelling pattern can be highly distorted by the background vorticity field associated with preexisting ocean features (Jaimes and Shay 2009, 2010).

Excess cooling produced by the control experiment in the southern cyclone is too large to ascribe to errors and biases in the blended SST product. To determine if the model initialization could have been a factor, the ocean heat content (OHC; Leipper and Volgenau 1972) referenced to the 26°C isotherm depth (D_{26}) derived from satellite altimetry, SST measurements, and ocean climatology (Mainelli et al. 2008) is compared to values calculated from initial model fields. Values for the southern cyclone are estimated over a 1° × 1° box centered at 25.0°N, 86.8°W. The derived OHC (D_{26}) value is 40 kJ cm^{-2} (48 m) while the initial model values are 25 kJ cm^{-2} (32 m). This initial cold bias may therefore have contributed to the overcooling. However, the detailed horizontal and vertical structures of ocean features provided by the initialization may also have influenced the upwelling pattern and its impact on cooling. Although it is possible that the vertical mixing parameterization could contribute to the overcooling, separating this contribution from others will be difficult. Future efforts to improve ocean model performance will depend heavily on the availability on detailed, high quality, three-dimensional ocean observations acquired prior to, during, and subsequent to individual storms to identify and separate the contributions of these different factors.

b. *Sensitivity to model attributes*

The sensitivity of the SST cooling pattern is evaluated by comparing SST changes from experiments GOM2–GOM15 to those from the control experiment GOM1. SST change is calculated for the control experiment as $\Delta T_C = (T_2 - T_1)_C$ and for each alternate experiment as $\Delta T_A = (T_2 - T_1)_A$, where T_1 (T_2) is the SST before (after) Ivan. The difference in SST change between each alternate experiment and the control experiment given by

$$\Delta T = \Delta T_A - \Delta T_C \tag{2}$$

is analyzed in Fig. 7, where the tabulated RMS amplitude of ΔT quantifies the similarity of each alternate experiment to the control experiment. Inset maps of ΔT are also presented in Fig. 7 for four of the alternate experiments. All statistics are calculated within the region outlined by the box in these four maps, which covers the eastern GOM and extreme northwest Caribbean Sea.

The simulated SST response is most sensitive to the alternate initialization (GOM14) with an RMS ΔT of 1.57°C. This large amplitude is evident in the inset map (Fig. 7). Large positive ΔT exists at the locations of the two cold-core cyclones because these features were not present in the alternate initialization. Substantial sensitivity to initialization extends beyond these ocean features and also beyond the region directly forced by the storm. Ocean model sensitivity to initialization is therefore likely to remain significant over other ocean regions

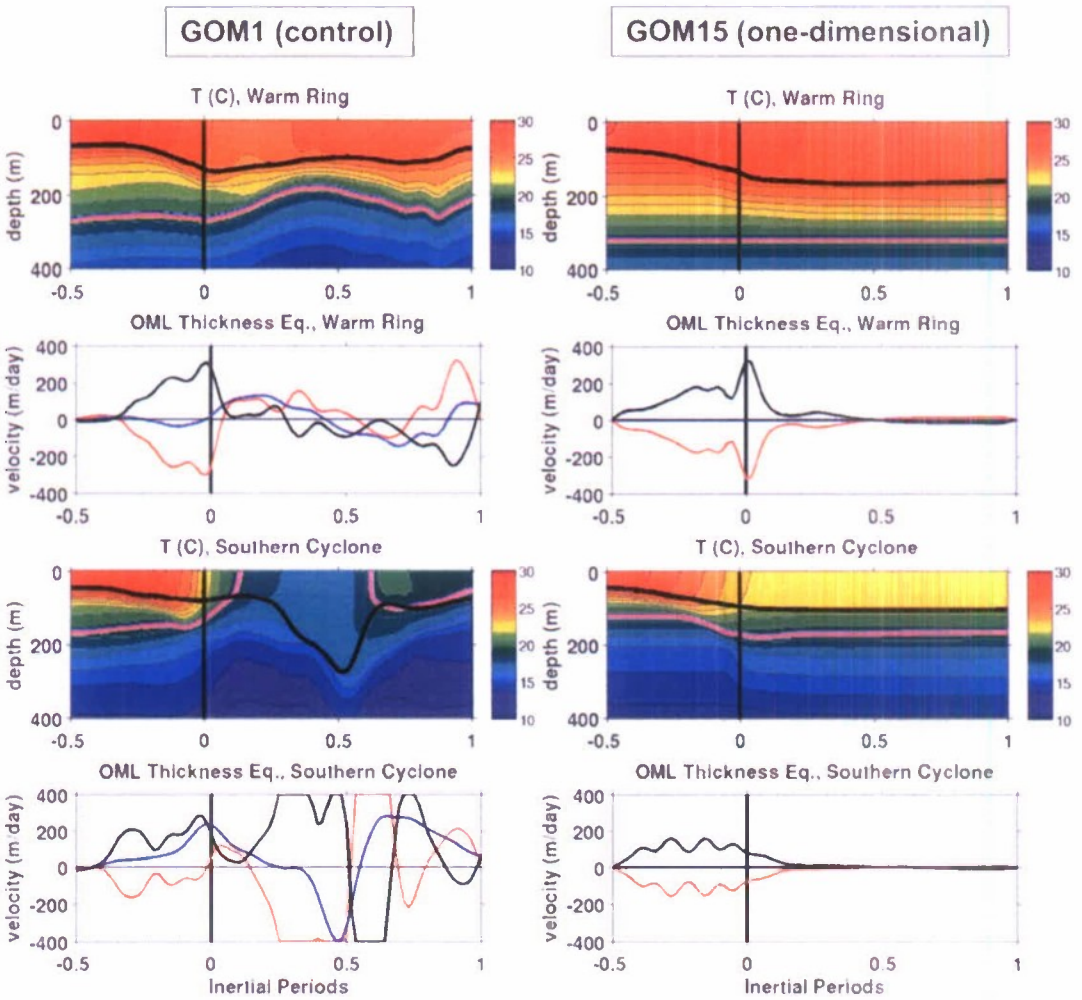

FIG. 6. (top row) Time series of temperature over the upper 400 m and (second row) of the three terms of Eq. (1) at a location in the detached warm ring. (bottom two rows) The same two plots at a location in the southern cold-core cyclone. (left) The control experiment GOM1 and (right) the one-dimensional experiment GOM15. These locations are illustrated by white dots in the top panel of Fig. 5. The thick black line denotes the OML base diagnosed as the depth where the temperature reaches 0.5°C below SST. The magenta line follows the 20°C isotherm in the depth–time temperature plots. For the terms in Eq. (1), w_E is the black line, w_M is the blue line, and $\partial z_M/\partial t$ is the red line.

with less energetic features. Even in the absence of energetic ocean features, it is still necessary to accurately initialize the temperature and salinity structure. The next largest sensitivity is observed for the ocean dynamics (GOM15) with an RMS ΔT of 1.31°C. At the other extreme, the SST response is least sensitive to vertical resolution (RMS ΔT of 0.29°C for low resolution and 0.26°C for high resolution), and also to turbulent heat flux drag coefficients (RMS ΔT of 0.18°C). In the latter case, the lack of sensitivity exists despite differences of about 30%–40% in values of C_{EL} and C_{ES} (Fig. 4). Although surface heat flux is expected to be sensitive to these different coefficient values (section 5), it has a relatively small influence on SST cooling, which mostly arises from entrainment across the OML base.

Intermediate ocean model sensitivity exists for the remaining attributes of horizontal resolution, vertical mixing, wind stress drag coefficient, and atmospheric forcing resolution. The exception to this is the small RMS ΔT value of 0.19°C realized for the Large and Pond C_D capped at high wind speed, which produced C_D values quite similar to those of Donelan used in the control experiment (Fig. 4). The inset ΔT map for GOM6 (GISS vertical mixing) along with the mean ΔT difference of 0.21°C (Fig. 7) demonstrates that this mixing scheme produces less SST cooling than KPP. The same is true for MY mixing (not shown). Parameterizations of C_D that produce larger (smaller) values result in greater (less) SST cooling. The inset map for GOM8 (Large and Pond C_D) reveals the enhanced SST cooling produced by this experiment (Fig. 7).

Alternate Experiment	Model Attribute Changed from Control Experiment	ΔT (C) Mean Diff.	ΔT (C) RMS
GOM2	Low horizontal resolution	+0.01	0.47
GOM3	Low vertical resolution	+0.05	0.29
GOM4	High vertical resolution	-0.02	0.26
GOM5	MY mixing	+0.06	0.49
GOM6	GISS mixing	+0.21	0.37
GOM7	Powell C_D	+0.13	0.33
GOM8	Large&Pond C_D	-0.19	0.48
GOM9	Large&Pond (capped) C_D	-0.08	0.19
GOM10	Shay&Jacob C_D	-0.39	0.75
GOM11	Jarosz *et al.* C_D	-0.04	0.28
GOM12	Kara *et al.* C_L, C_S	-0.13	0.18
GOM13	No H*WIND	+0.25	0.70
GOM14	Outer model	+0.43	1.57
GOM15	One-dimensional	-0.17	1.31

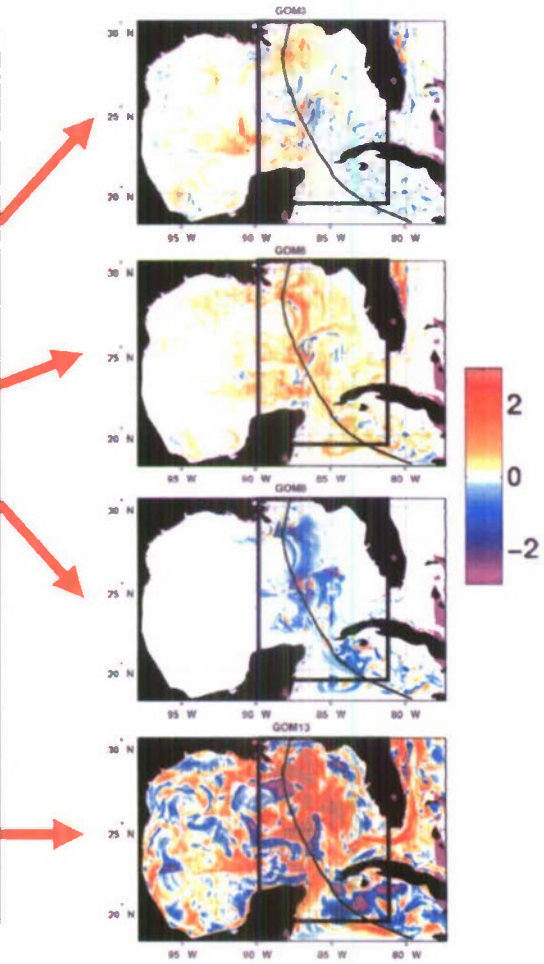

FIG. 7. Sensitivity analysis of the SST change forced by Hurricane Ivan (track is black line), as summarized by differences in the SST change (17 − 11 Sep) calculated using Eq. (2) between the control experiment GOM1 and each of the remaining experiments GOM2–GOM15. The RMS amplitude of ΔT (°C), which represents the RMS difference between the SST changes forced by the two experiments, is tabulated in the third column. Four ΔT maps are shown as examples. All RMS ΔT values are calculated within the rectangular boxes outlined by black lines in the maps (extreme NW Caribbean Sea and eastern GOM).

Enhanced cooling is also produced by GOM10 (Shay and Jacob C_D) while the opposite is true for GOM7 (Powell C_D). This relationship results from differences in the strength of wind-driven turbulence resulting from changes in surface friction velocity and, also, from changes in the magnitude of wind-driven flow that impact the magnitude of both upwelling and shear at the OML base.

A Taylor (2001) diagram (Fig. 8, top) is used to compare the ΔT_A from each alternate experiment to the ΔT_C over the subdomain covering the eastern GOM and extreme northwest Caribbean Sea, specifically the box outlined in the Fig. 7 inset maps. To construct this diagram, the mean is first removed from each ΔT_A and ΔT_C map, and then all maps are normalized by the variance of ΔT_C. This diagram is effective because each point simultaneously represents three different metrics. The large black square in the diagram is the point that signifies a perfect comparison (correlation coefficient of 1.0, identical normalized RMS amplitude of 1.0, and RMS difference of zero between maps). One plotted point quantifies the similarity between ΔT_A and ΔT_C, with the RMS amplitude of ΔT_A given by the radial distance from the plot origin at the bottom-left corner, the RMS difference between the two fields being proportional to the linear distance between the plotted point and the large black square, and the correlation coefficient being a function of the direction angle of the vector connecting the plot origin with the plotted point.

The greatest sensitivity again results from the alternate initialization (GOM14), which has a (correlation, normalized RMS amplitude, normalized RMS difference) of (0.59, 0.58, 0.81) with respect to the control experiment (Fig. 8). The small RMS amplitude of 0.58 is due largely to the absence of the two cyclones directly hit by Ivan and the associated large cooling. The

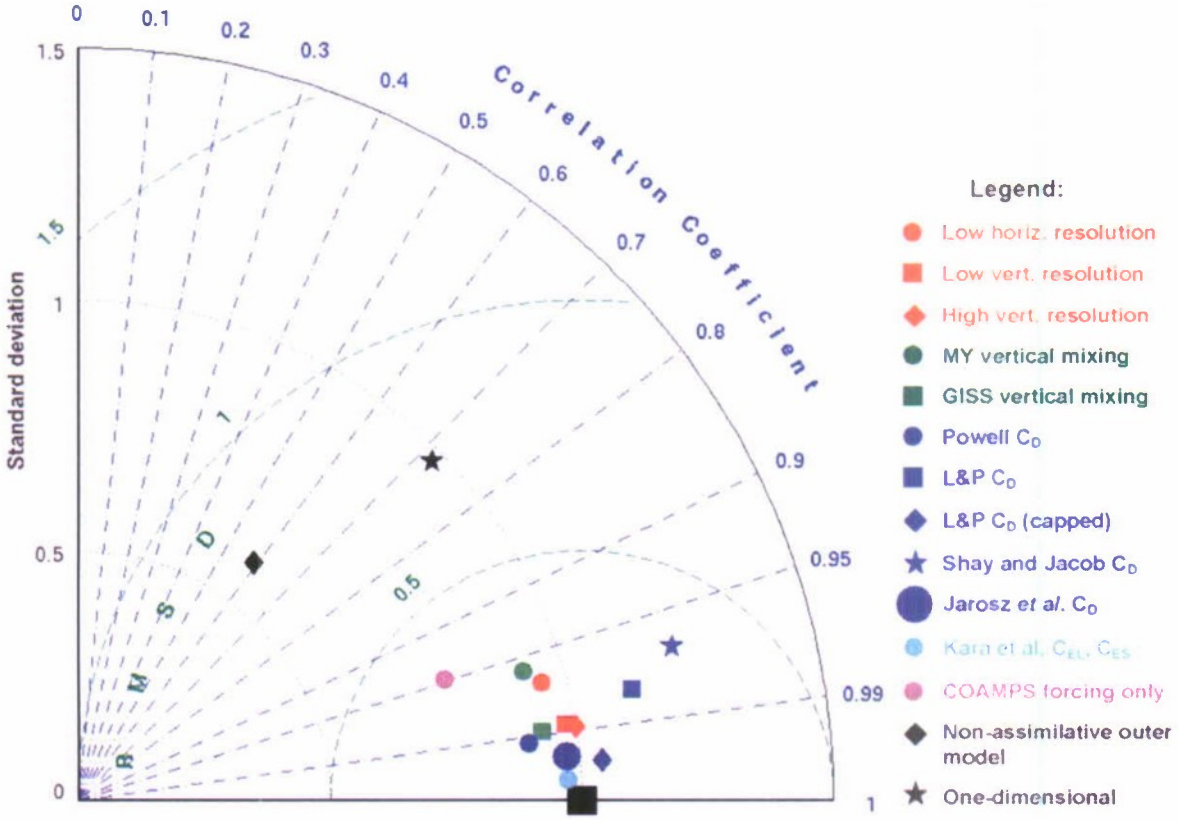
Correlation Coefficient
Standard deviation
0
0.1
0.2
0.3
0.4
0.5
0.6
0.7
0.8
0.9
0.95
0.99
1
1.5
1
0.5
0
RMS
Legend:
Low horiz. resolution
Low vert. resolution
High vert. resolution
MY vertical mixing
GISS vertical mixing
Powell C_D
L&P C_D
L&P C_D (capped)
Shay and Jacob C_D
Jarosz *et al.* C_D
Kara et al. C_{EL}, C_{ES}
COAMPS forcing only
Non-assimilative outer model
One-dimensional

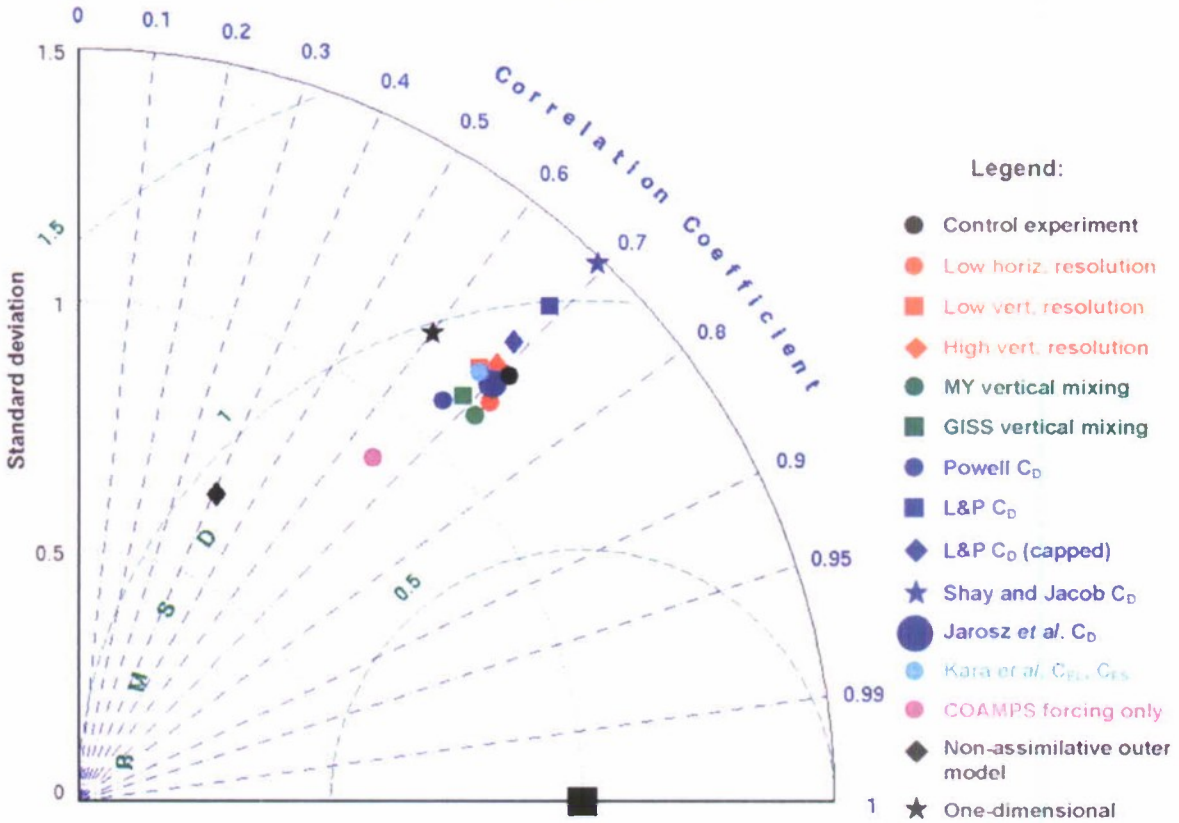
Correlation Coefficient
Standard deviation
0
0.1
0.2
0.3
0.4
0.5
0.6
0.7
0.8
0.9
0.95
0.99
1
1.5
1
0.5
0
RMS
Legend:
Control experiment
Low horiz. resolution
Low vert. resolution
High vert. resolution
MY vertical mixing
GISS vertical mixing
Powell C_D
L&P C_D
L&P C_D (capped)
Shay and Jacob C_D
Jarosz *et al.* C_D
Kara et al. C_{EL}, C_{ES}
COAMPS forcing only
Non-assimilative outer model
One-dimensional

one-dimensional experiment (GOM15) has a (correlation, normalized RMS amplitude, normalized RMS difference) of (0.72, 0.97, 0.72) with the control experiment. All other alternate experiments are highly correlated with the control experiment (≥0.95, Fig. 8), demonstrating that correct model initialization and three-dimensional ocean dynamics are necessary to accurately predict the SST response. At the other extreme, the three experiments displaying the least SST sensitivity are GOM12 (alternate turbulent heat flux parameterization), GOM9 (Large and Pond C_D capped at high wind speed), and GOM15 (Jarosz et al.). The dependence of RMS amplitude on C_D is evident as is the several-percent reduction in RMS amplitude produced by the two alternate vertical mixing choices. RMS amplitude produced by GOM13 (no H*WIND blending) is reduced by ≈25% due to the highly smoothed representation of inner-core storm structure and the resulting reduction in maximum wind speed.

Since these comparisons are substantially influenced by the large cooling that occurred within the two oceanic cyclones, the focus now shifts to the cooling that occurred in these features (Table 2). The largest underestimate of cooling relative to the control experiment is produced by GOM14 within the southern cyclone where the post-Ivan SST is 6.9°C warmer than in GOM1 because of the absence of this feature. The inadequate resolution of storm structure by the alternate forcing (GOM13) and the absence of three-dimensional ocean dynamics (GOM15) each led to reduced cooling of 1.0°–3.2°C in both cyclones (Table 2). The two alternate vertical mixing choices reduce the SST cooling relative to the control by 0.6°–1.8°C while C_D parameterizations that produce larger (smaller) values than the Donelan et al. (2004) choice over intermediate to high wind speeds increase (decrease) the cooling by up to 0.9°C (1.5°C). Little difference in cooling results from altering the horizontal and vertical resolutions or from altering the turbulent heat flux drag coefficients.

c. *Evaluation of the SST response against the blended SST fields*

To evaluate the realism of the SST cooling pattern from all experiments against the observations, a Taylor diagram analysis compares ΔT_A and ΔT_C maps from all 15 experiments to ΔT_R maps calculated from the blended SST analysis over the subdomain outlined in the Fig. 7 inset maps. In this case, all maps are first normalized by the variance of the ΔT_R map. This evaluation is supplemented by calculating both the mean differences and the RMS differences over the same subdomain (Table 3). The mean differences provide information that is not contained in the Taylor diagram while the RMS differences document the dimensional magnitude of the nondimensional RMS differences that appear in the diagram. The evaluation is also supplemented by the Murphy (1988) skill score S, given by

$$S = r^2 - \left[r - \left(\frac{\sigma_Y}{\sigma_X}\right)\right]^2 - \left[\left(\frac{\overline{Y} - \overline{X}}{\sigma_X}\right)\right]^2, \qquad (3)$$

where $\overline{X}$ and $\overline{Y}$ are the mean values of fields X and Y, σ_X and σ_Y are their standard deviations, and r is the correlation coefficient between them. If the two maps are identical, then $S = r^2$; otherwise, $S < r^2$. This score is reduced by three factors: 1) correlation, 2) differences in

TABLE 3. Comparison of ΔT maps (17 − 10 Sep) between the 15 experiments and the blended SST: mean difference (column 1), RMS difference (column 2), and Murphy skill score S from Eq. (3) (column 3). Skill scores are also presented for u and v profiles at SEED mooring 9.

Expt	ΔT mean diff (°C)	ΔT RMS diff (°C)	ΔT skill score	$u(z, t)$ skill score	$v(z, t)$ skill score
GOM1	0.24	1.33	0.20	0.71	0.77
GOM2	0.25	1.29	0.27	0.64	0.73
GOM3	0.30	1.40	0.12	0.65	0.78
GOM4	0.22	1.40	0.17	0.63	0.78
GOM5	0.30	1.26	0.28	0.62	0.61
GOM6	0.47	1.33	0.07	0.71	0.68
GOM7	0.38	1.33	0.14	0.58	0.60
GOM8	0.04	1.57	−0.02	0.47	0.54
GOM9	0.14	1.47	0.12	0.61	0.74
GOM10	−0.19	1.71	−0.19	0.45	0.26
GOM11	0.06	1.37	0.27	0.66	0.74
GOM12	0.11	1.34	0.22	0.70	0.76
GOM13	0.51	1.24	0.10	0.42	0.22
GOM14	0.84	1.51	−0.61	0.21	0.65
GOM15	0.06	1.55	0.04	−1.10	−0.97

←

FIG. 8. (top) Taylor diagram comparing ΔT calculated using Eq. (2) from the control experiment to ΔT from all remaining experiments. Symbols representing the different experiments are labeled in the legend. Different symbol colors in the diagram and in the legend categorize the individual model attributes that are varied: horizontal and vertical resolutions (red), vertical mixing choice (green), wind stress drag coefficient (blue), turbulent heat flux coefficient (cyan), atmospheric forcing resolution (magenta) and outer model choice (black diamond). The large black square at a correlation of 1.0 and an RMS amplitude of 1.0 represents a perfect comparison. (bottom) Taylor diagram comparing ΔT calculated for each experiment to the observed ΔT estimated from the Reynolds SST analysis. As shown in the legend at the bottom, symbols and colors follow the same conventions except that the control experiment is included as a black circle. The large black square again represents a perfect comparison.

the mean, and 3) differences in the RMS amplitude. Values exceeding 0 represent statistically significant skill.

In the Taylor diagram (Fig. 8, bottom), the control experiment has a (correlation, normalized RMS amplitude, normalized RMS difference) of (0.71, 1.20, 0.86) (see Table 3 for the corresponding dimensional RMS difference). The resulting skill score $S = 0.20$ is significant but not large due to the 20% amplitude overestimate and also to the RMS difference values that are nearly as large as the RMS amplitudes of the two fields (Table 3). Eleven of the 15 experiments produce correlation coefficients between 0.67 and 0.72, with alternate model attributes primarily influencing normalized RMS amplitudes. The dependence of RMS amplitude on the value of C_D is particularly evident (Fig. 8, Table 3). The two experiments using the largest values of C_D (GOM8, GOM10) produced negative S. Of the remaining three experiments, the alternate initialization experiment GOM14 is the largest outlier, with (correlation, normalized RMS amplitude, normalized RMS difference) of (0.41, 0.66, 0.97) and insignificant S. The alternate forcing experiment GOM13 produces a substantially smaller normalized RMS amplitude (0.88) than most other experiments along with a slightly reduced correlation of 0.65 and small but significant $S = 0.10$. One-dimensional dynamics (GOM15) results primarily in a modest reduction in correlation to 0.61 but with a very small $S = 0.04$. Overall, the experiments overestimate the amplitude of the SST change pattern forced by Ivan by ≈20% compared to the blended SST analysis, which probably results to a large extent from the large overcooling in the southern cyclone.

The mean differences listed in Table 3 demonstrate that in the subdomain over which these analyses were performed, the ocean model did not cool as much as was shown in the blended SST fields. Although the model tended to substantially overcool in the cyclones, this was more than compensated for by undercooling over the remainder of the domain. Mean differences display the largest sensitivity to ocean model initialization, surface forcing resolution, and wind stress drag coefficient, with more (less) cooling occurring for larger (smaller) values of C_D. Smaller sensitivity is evident for the vertical mixing choice, with the MY and GISS schemes producing slightly more cooling than KPP. Little sensitivity is evident to the vertical and horizontal resolutions. These conclusions also generally hold for SST cooling within the two cyclones (Table 2).

5. Thermal energy provided by the ocean to the storm

a. Estimation procedure

Although the accuracy of SST forecasts is important, it is the influence of SST cooling on surface turbulent heat flux that most directly impacts TC intensity. It is not possible to evaluate SST cooling relative to Ivan's center against observations as it propagates because satellite sampling is restricted by the cloud cover and heavy precipitation. For these reasons, we do not attempt to evaluate the accuracy of SST cooling following the storm. Instead, we document the sensitivity of the surface turbulent heat flux to model attributes by averaging the flux within a specified radius of the storm center and graphing it along the storm path. The choice of averaging radius is important because it should include the area of the ocean surface that is actually providing the large majority of thermal energy to the storm. Since this choice is uncertain (e.g., Shen et al. 2002; Cione and Uhlhorn 2003), sensitivity analysis is performed for two different radii: $1.4R_{MAX}$ and $3R_{MAX}$, where R_{MAX} is the radius of maximum wind. These choices are illustrated in the blended wind speed forcing map (Fig. 2), where $1.4R_{MAX}$ encloses the region influenced by the eyewall, while $3R_{MAX}$ encloses most of the region influenced by hurricane force winds. The surface turbulent heat flux Q_T averaged over these two radii is graphed as a function of storm latitude for all experiments in Fig. 9. Although this type of sensitivity analysis is most appropriately performed with a coupled model that produces atmospheric feedback, it is still important to understand how ocean model attributes alone influence the oceanic contribution to surface turbulent heat flux through differences in SST cooling.

b. Sensitivity analysis

The progression of mean Q_T along the storm path in the control experiment is strongly influenced by the oceanographic features. Over the northwest Caribbean and the LC (south of 23°N), mean Q_T within $1.4R_{MAX}$ of the storm center averages about -600 W m^{-2}. When the storm encounters the two cold cyclones, SST cooling inside the averaging radius is sufficiently rapid to produce positive (sensible only) turbulent heat flux from the atmosphere to the ocean as SST becomes colder than air temperature. This impact of the cyclones is likely exaggerated because the air temperature used to force the model is fixed and the atmospheric feedback cannot occur. Some atmospheric feedback is present in the COAMPS air temperature forcing fields since it was coupled to an ocean model, but the air temperature probably remains too high because the coarse representation of Ivan in the COAMPS atmospheric model presumably generated insufficient SST cooling. Experiment GOM13 (no H*WIND blending) is consistent with this hypothesis since it underestimated SST cooling in the cold-core cyclones by ≥2°C (Table 2). Despite this exaggerated flux reversal, it remains clear that thermal energy provided by the ocean to the inner-core region of Ivan is very sensitive to the presence of these

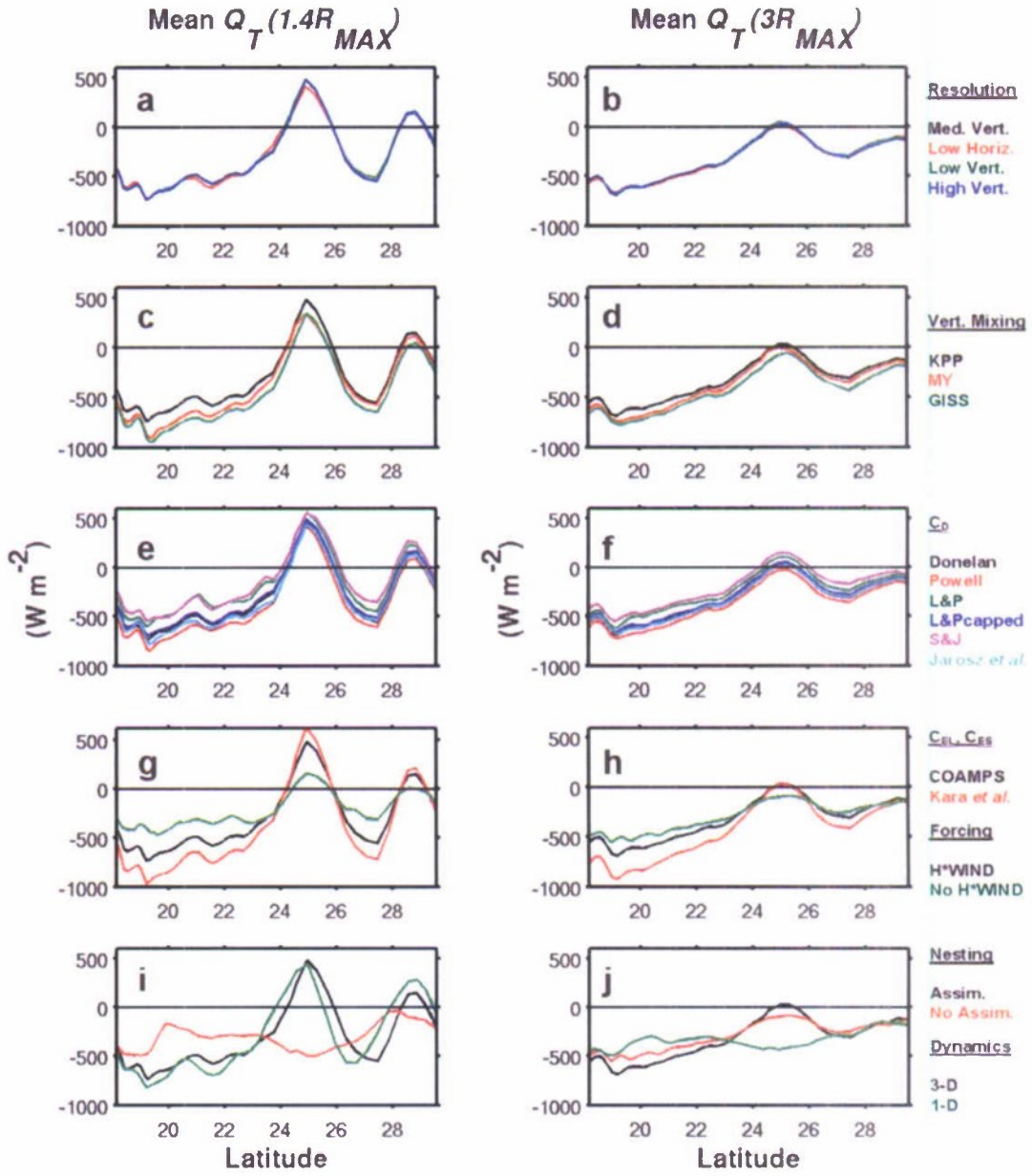

FIG. 9. Air–sea thermal heat flux averaged over (left) $1.4R_{MAX}$ and (right) $3.0R_{MAX}$ following the path of the storm and graphed as a function of storm central latitude. In each panel, the control experiment is compared to alternate experiments representing a particular category of model attribute being varied: model resolution (top row), vertical mixing choice (second row), wind stress drag coefficient (third row), turbulent heat flux drag coefficients (fourth row), and both surface forcing resolution and the outer model used for nesting (bottom row). The control experiment is represented by the black line in all panels. Colors representing other experiments are shown in the legends at right. Negative values indicate heat flux from the ocean to the atmosphere.

warm and cold ocean features. The progression of Q_T over the larger $3R_{MAX}$ averaging region is similar over the northwest Caribbean and the LC, but the change in Q_T as the storm passes over the two cyclones is substantially reduced because warmer water outside of the two cyclones is included in the averaging region. The flux is near 0 over the southern cyclone and remains negative (ocean to atmosphere) over the northern one.

Little sensitivity of Q_T to either the horizontal or vertical grid resolutions exists for both averaging radii (Figs. 9a and 9b), but substantial sensitivity exists for all other model attributes. Focusing on the $1.4R_{MAX}$ averaging area, altering the vertical mixing algorithm produces differences up to 200 W m^{-2} (20%–30%) over the northwest Caribbean Sea and LC in the GOM (Fig. 9c). Altering either the wind stress or turbulent heat flux drag

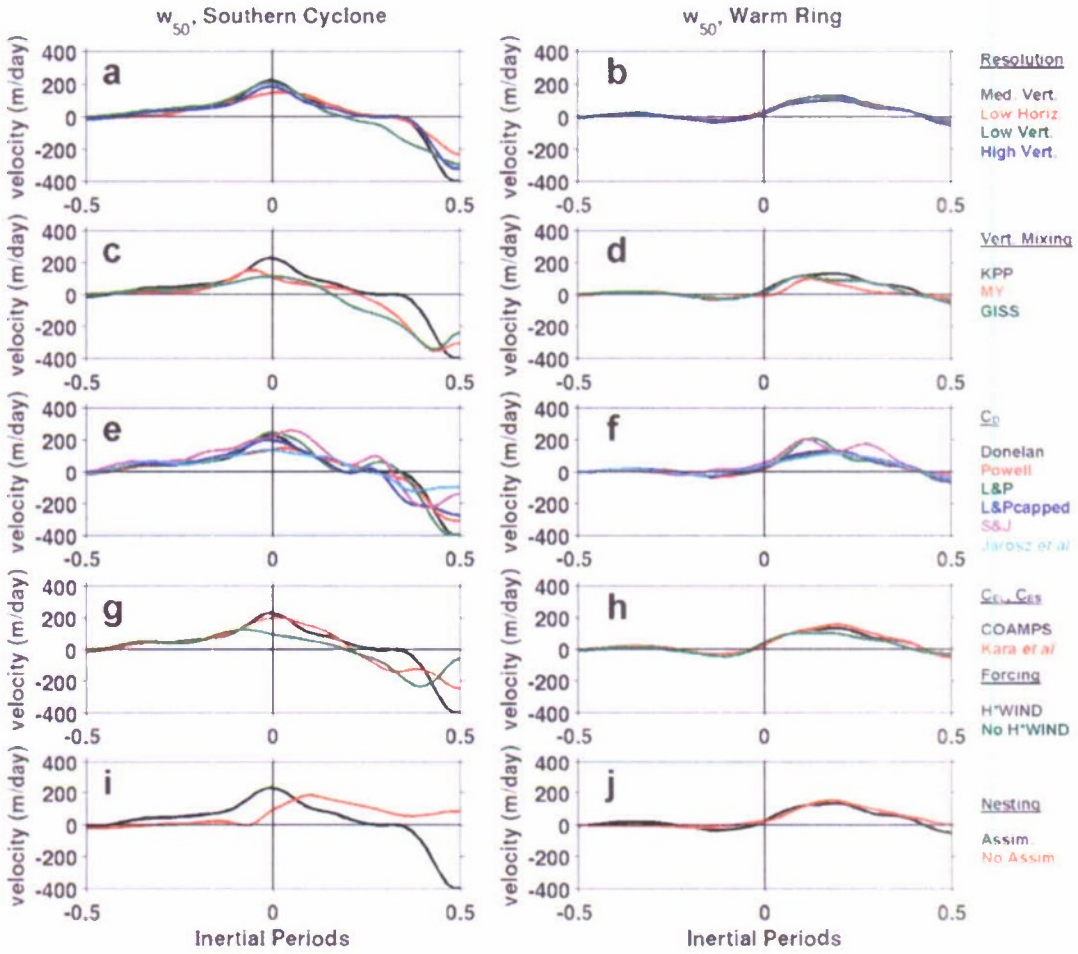

FIG. 10. Time series of w_{50} at (left) a location in the eastern part of the southern cold cyclone and (right) the eastern side of the warm ring at the two locations shown in the top panel of Fig. 5. The experiments are sorted into separate panels based on the type of model attribute as in Fig. 9. The control experiment is represented by the black line in all panels. Colors representing other experiments are shown in the legends at right.

coefficients produces larger differences of up to 300 W m^{-2} (30%–40%) for C_D (Fig. 9e) and 250 W m^{-2} (25%–30%) for C_{EL} and C_{ES} (Fig. 9g). Although heat flux sensitivity to changes in C_{EL} and C_{ES} is large, SST is insensitive since surface heat flux does not make a leading-order contribution to the SST change based on results from earlier studies (e.g., Jacob et al. 2000; Shay and Jacob 2006). Large sensitivities are observed as expected for both the low-resolution forcing and the alternate model initialization experiments (Fig. 9i). Except for turbulent flux drag coefficients, changes in model attributes that cool SST faster produce reduced heat loss to the atmosphere as expected.

Sensitivity results are generally similar over the larger $3R_{MAX}$ averaging radius. However, over the northwest Caribbean Sea and LC in the GOM, the differences that result from altering the vertical mixing and wind stress drag coefficient are smaller than the differences over the smaller averaging radius (Fig. 9d and 9f). The sensitivity of surface heat flux to altering the model attributes is greatest in the inner-core region of the storm. The impacts on hurricane intensity will therefore depend on the poorly known radial distance within which the ocean actually provides thermal energy to the storm (Shen et al. 2002; Cione and Uhlhorn 2003).

6. Ocean dynamics

a. Sensitivity of vertical velocity to model attributes

Given that vertical advection can contribute significantly to SST cooling, the sensitivity of vertical advection to changes in he model attributes is assessed by graphing the vertical velocity at 50-m depth (w_{50}) as a function of time (Fig. 10) at the same two locations (warm anticyclone and southern cyclone) where the impacts of vertical

velocity on SST cooling were analyzed in Fig. 6. The only difference is that w_{50} sampled by the synthetic instruments is vertically interpolated to 50 m instead of the OML base. The behavior of w_{50} in the control experiment is consistent with the results summarized in Fig. 6, with maximum positive w_{50} occurring near the time of Ivan's passage in the southern cyclone and with somewhat weaker maximum positive w_{50} lagging passage by a few hours along the eastern periphery of the warm anticyclone.

The interpretation of sensitivity in Fig. 10 is confined to the time interval when direct forcing by Ivan was important (roughly ±3 IP). The least sensitivity in w_{50} is due to the altered vertical resolutions in both ocean features. Sensitivity to horizontal resolution is small except in the cyclone where it is reduced by about 30% at the time of maximum forcing. Little sensitivity is evident when C_{EL} and C_{ES} are changed as expected due to the lack of SST sensitivity. When other model attributes are altered, maximum w_{50} can vary by 50% or more in the southern cyclone. This sensitivity is sufficiently large that differences in the upwelling response beneath the inner core of Ivan could contribute significantly to differences in SST cooling. By comparison, substantially less sensitivity is observed in the warm ring for all model attributes. In this ocean feature, a sharp peak in upwelling velocity is observed 0.1 IP after storm passage for the two experiments that used the uncapped Large and Pond and the Shay and Jacob C_D parameterizations, presumably related to the fact that these choices have large values at high wind speed. A secondary peak is observed at 0.3 IP for the Shay and Jacob choice, which is possibly related to the fact that this choice has comparatively large values at the intermediate wind speeds found in the outer reaches of the storm.

b. *Velocity profiles produced by the control experiment*

ADCP observations from SEED moorings 1, 3, 7, and 9 are used to evaluate the capability of the control experiment to simulate the wind-driven near-inertial current response (Teague et al. 2007), which is critically important to the shear-driven turbulent entrainment at the OML base. The u and v components at these moorings are shown for the upper 150 m of the water column over a time interval ranging from 0.5 IP before the storm to 1.5 IP after passage, which represents the forced response and the subsequent transition to near-inertial current variability (Fig. 11). Observed velocity components are graphed over the same time–depth range except for the near-surface region where the ADCP could not sample velocity because of sidelobe interference. The responses at moorings 7 and 9 where the water depths (>500 m) are much greater than the OML thickness are dominated by forced, near-inertial waves, and the simulated response closely resembles the observed response over their common depth range. The magnitude of the response at mooring 7 is reduced by the unfavorable anticlockwise rotation of the wind stress vector as Ivan passes. These observations and simulations suggest that vertical energy propagates out of the surface mixed layer and into the thermocline in a manner consistent with theory. At both moorings, westward mean flow is present in the u field while the mean v is near 0.

Although the near-inertial time scales of the response at shallow-water (50 m) moorings 1 and 3 are generally evident, the response is more complicated than in deeper water. The v response at mooring 1 displays strong mid-depth northward flow between 0.5 and 1 IP following storm passage that is captured in the model current response. The observed u and v responses at mooring 3 reveal a relatively strong northeastward flow event in the bottom 10 m around 0.5 IP after storm passage that is not captured by the model. Without observations of the three-dimensional ocean structure in the vicinity of these moorings, we cannot determine the reason for this near-bottom flow event or why the model did not reproduce it. Overall, however, the resemblance between the observations and simulations at these moorings is encouraging, particularly for the deeper moorings.

c. *Sensitivity of velocity profiles to model attributes*

A Taylor diagram is used to quantify the sensitivity at SEED mooring 9 by comparing the v fields from each alternate experiment to the v generated by the control experiment (Fig. 12, top). To construct this diagram, the mean was first removed from each v field over the time interval between −0.5 and 1.5 IP and over the upper 150 m. The resulting two-dimensional fields were normalized by the variance of the field from the control experiment. In contrast to the situation farther offshore, the alternate initialization (GOM14) is not an outlier for simulated velocity. The initial flow at SEED mooring 9 is westward in both GOM14 and GOM1 (Fig. 11), so the different initializations produced similar background flows in this region.

The greatest outliers in the mooring 9 sensitivity analysis are the low-resolution atmospheric forcing experiment GOM13 and the one-dimensional experiment GOM15. In GOM13, velocity amplitude is underestimated by up to 40% relative to the control experiment. The correlation with this control experiment is also reduced to 0.9, primarily because the weaker forced currents do not penetrate as deep into the water column (not shown). In GOM15, velocity amplitude is overestimated by >40% and the correlation with the control experiment is reduced to 0.66 because the response is purely inertial and energy does not penetrate into the ocean interior through near-inertial wave dynamics (Shay and Elsberry 1987; Shay et al. 1989).

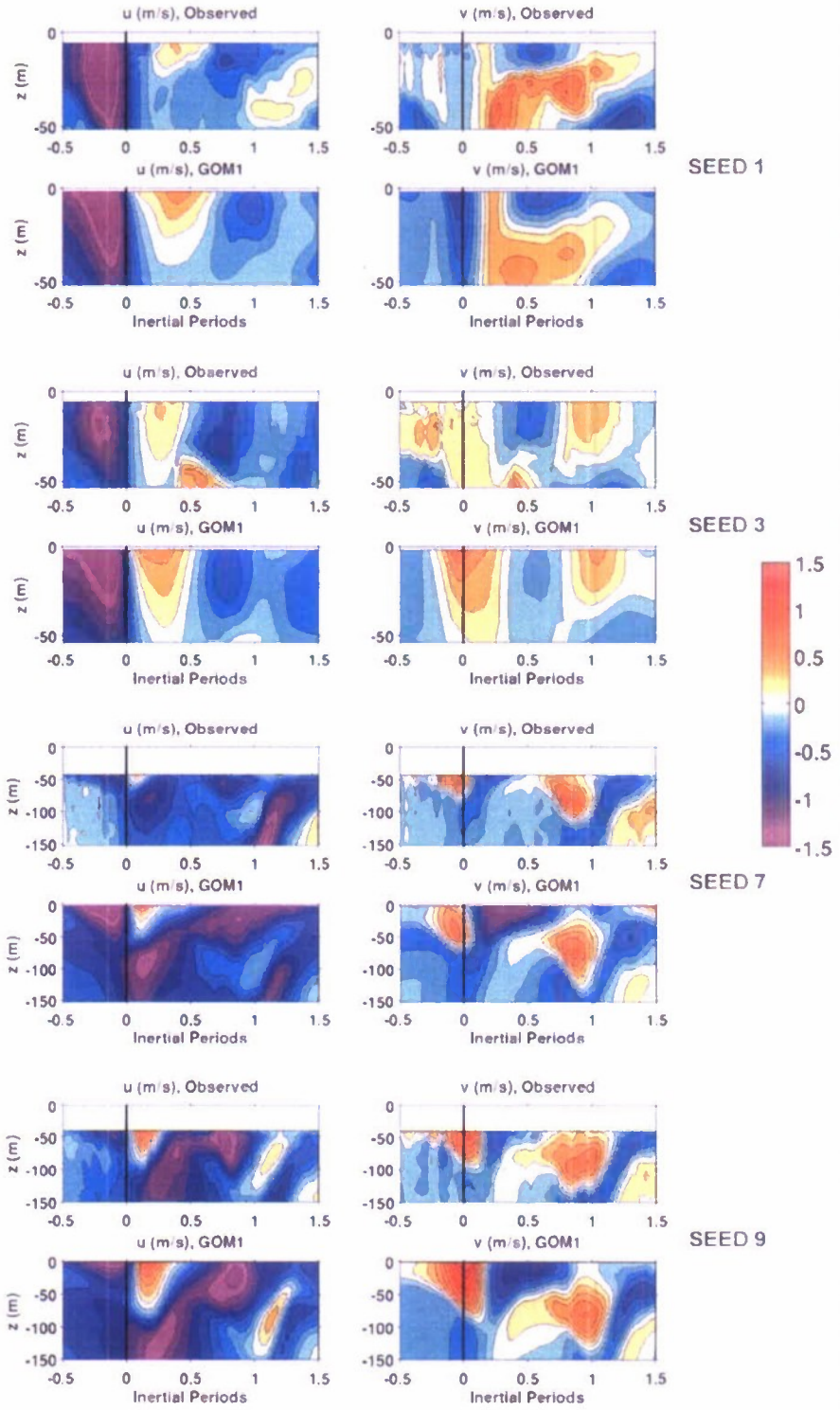

FIG. 11. Time series of (left) u and (right) v over the upper 150 m from both the observations and the control experiment GOM1 at (top to bottom) SEED moorings 1, 3, 7, and 9. The time axis has been scaled to the local IP from the time of closest approach of the storm center.

The correlation is also reduced because GOM15 produces current fluctuations with an exactly inertial period while GOM1 produces fluctuations with a period about 10% smaller than inertial (Fig. 11). The impacts of upwelling on OML thickening are also absent in GOM15.

The next greatest level of sensitivity results from altering the wind stress drag coefficient. The choices that produce larger (smaller) C_D values produce larger (smaller) RMS amplitudes than the control experiment. Both increased and decreased C_D are associated with a reduction in correlation, primarily because increased (decreased) C_D is associated with increased (decreased) penetration of the wind-forced currents deeper into the water column (not shown). Two choices of C_D (Large and Pond capped, GOM9; Jarosz et al., GOM11) display little difference from the control experiment. These results are generally consistent with simulations of the ocean response to Hurricane Francis (2004) by Sanford et al. (2007), who determined that runs with C_D values capped or reduced at high wind speeds outperformed runs using the uncapped Large and Pond representation. Low sensitivity is observed with altering vertical mixing choice and with both vertical and horizontal resolutions. The alternate heat flux coefficient experiment produces fluctuations that are nearly identical to the control experiment, as expected.

d. *Evaluation of velocity profiles against observations*

A Taylor diagram analysis is performed to compare v fluctuations at SEED mooring 9 produced by all 15 experiments to the observed fluctuations (Fig. 12, bottom). It is conducted over the common depth range of 40–150 m and from 0.5IP before to 1.5IP after the storm. All fields are normalized by the variance of the observed v fluctuations. This analysis is supplemented by skill scores calculated over the same depth–time range (Table 3). The control experiment produces one of the most realistic simulations of upper-ocean v fluctuations with (correlation, normalized RMS amplitude, normalized RMS difference) of (0.89, 1.46, 0.48) and with skill scores of 0.71 and 0.77 for u and v, respectively.

Vertical resolution, the turbulent heat flux drag coefficient, and both the capped Large and Pond and Jarosz et al. choices of wind stress drag coefficient all have only a minor impact on the quality of the response while horizontal resolution has only a slightly larger influence. The vertical mixing choice has a substantial influence on the magnitude of the current, with both the MY and GISS experiments (GOM5 and GOM6) producing a substantially weaker velocity response. This result contrasts with the sensitivity evaluation in Fig. 12 (top) where the other vertical mixing choices produced velocity fluctuations with magnitudes close to that of the control experiment. This difference occurred because the present comparison to the observations is limited to the depth range between 40 and 150 m, suggesting that the forced velocity fluctuations in GOM5 and GOM6 are more surface intensified and do not penetrate downward into the water column as effectively as they do in the control experiment. Consequently, the KPP mixing choice produces a more realistic current response with respect to these observations. The wind stress drag coefficient has a significant impact on the predicted velocity profile. The choices of C_D other than Large and Pond capped and Jarosz et al. degraded the overall realism of the simulated velocity fluctuations. The two parameterizations that continue to increase in value at high wind speeds produced less-realistic velocity responses, in agreement with Sanford et al. (2007). The two most unrealistic simulations (GOM13 and GOM15) were poorly correlated with the observations and had low skill scores (Table 3).

Taylor diagrams comparing the simulated v responses to the observations are also presented for moorings 1 and 7 (Fig. 13). In general, the conclusions reached from v at mooring 9 (Fig. 12, bottom) are upheld, in particular the dependence on the C_D choice. Comparisons are again poor for low-resolution forcing (GOM13) and for one-dimensional ocean dynamics (GOM15). For the most realistic experiments, the quality is slightly reduced in comparison to mooring 9 due to the weaker response to the west of the eye. A further reduction in quality is evident over the shelf with maximum correlations close to 0.7 as opposed to between 0.8 and 0.9 farther offshore.

7. Conclusions

The response of an ocean model to Hurricane Ivan (2004) has been documented in the GOM and NW Caribbean Sea. The sensitivity of the simulated response to changes in several specific attributes of the model (Table 1) was quantified and the realism of the model response was evaluated against SST images derived from satellite and in situ measurements along with upper-ocean current profiles measured at ADCP moorings. Key results are summarized in Table 4, along with recommendations for each model attribute. In drawing conclusions from these results, it must be kept in mind that they are representative of one particular storm in one distinct ocean region, and have been obtained from a stand-alone ocean model without atmospheric feedback that was driven by quasi-optimal but imperfect atmospheric forcing. Despite these limitations, the present study represents a baseline effort to understand the strengths and limitations of ocean models with respect to their numerics and parameterizations, a first step toward the ultimate goal of improving their performance in coupled forecast models. It provides

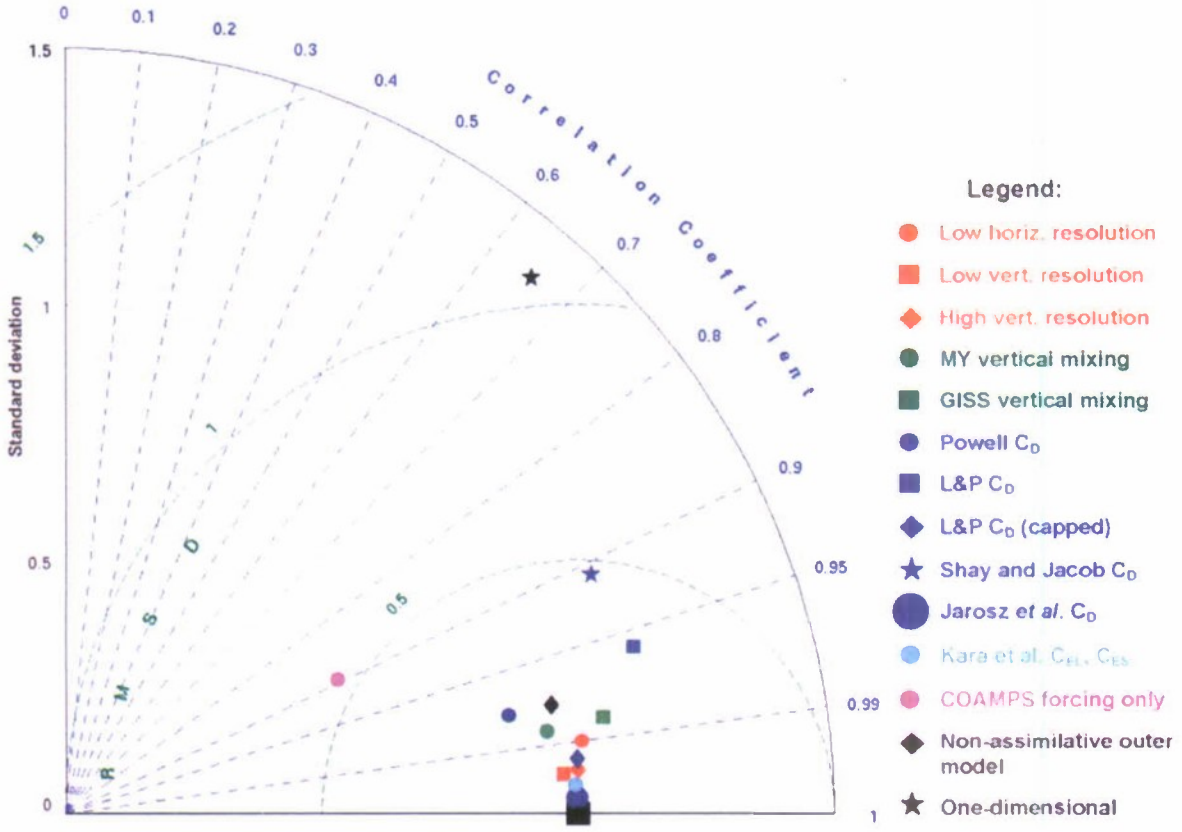
Correlation Coefficient
Standard deviation
0
0.1
0.2
0.3
0.4
0.5
0.6
0.7
0.8
0.9
0.95
0.99
1
1.5
0.5
RMSD
Legend:
Low horiz. resolution
Low vert. resolution
High vert. resolution
MY vertical mixing
GISS vertical mixing
Powell C_D
L&P C_D
L&P C_D (capped)
Shay and Jacob C_D
Jarosz *et al.* C_D
Kara et al. C_{EL}, C_{ES}
COAMPS forcing only
Non-assimilative outer model
One-dimensional

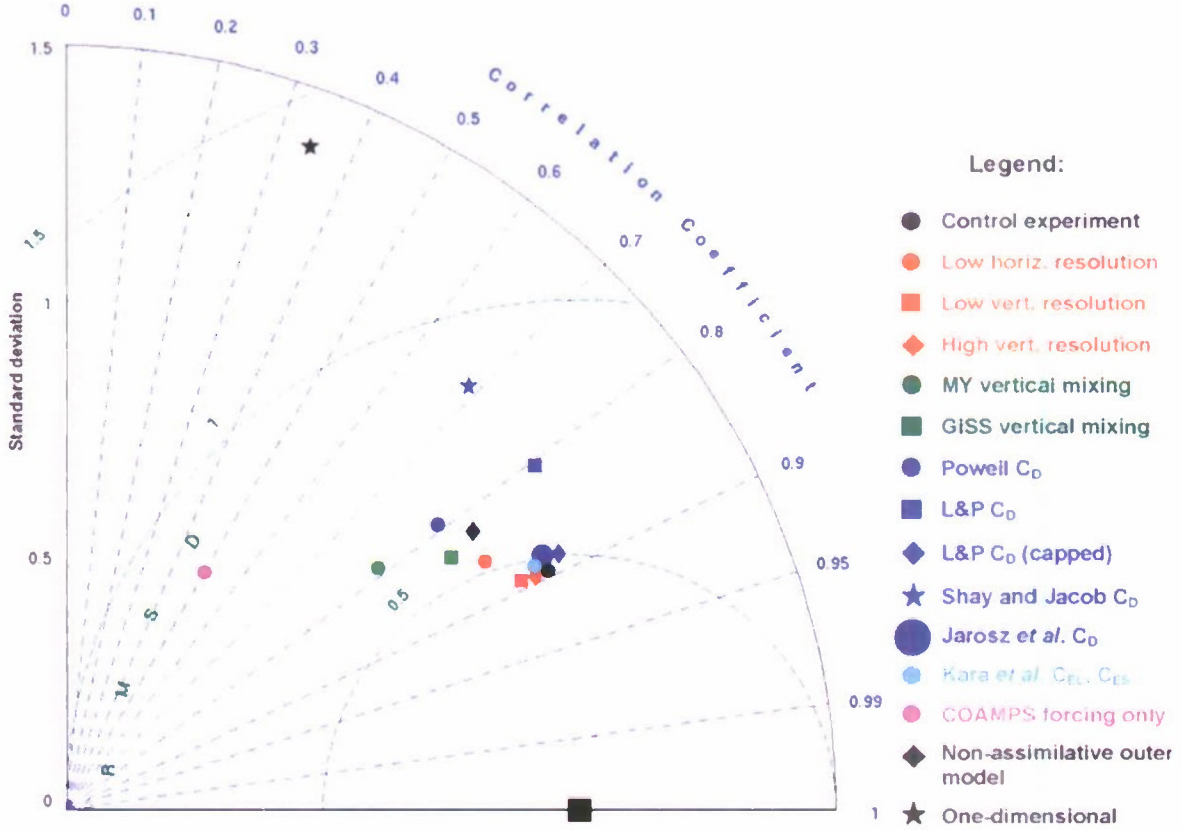
Correlation Coefficient
Standard deviation
0
0.1
0.2
0.3
0.4
0.5
0.6
0.7
0.8
0.9
0.95
0.99
1
1.5
0.5
RMSD
Legend:
Control experiment
Low horiz. resolution
Low vert. resolution
High vert. resolution
MY vertical mixing
GISS vertical mixing
Powell C_D
L&P C_D
L&P C_D (capped)
Shay and Jacob C_D
Jarosz *et al.* C_D
Kara et al. C_{EL}, C_{ES}
COAMPS forcing only
Non-assimilative outer model
One-dimensional

guidance toward where we should most effectively invest our efforts to improve model performance.

The present results demonstrate that representation of the ocean by one-dimensional ocean models may be inadequate for predicting the ocean response to some storms. In the region studied in this analysis, energetic ocean features such as the LC and eddies distort the wind-driven momentum response and the associated upwelling patterns that can significantly influence SST cooling beneath a storm (e.g., Jaimes and Shay 2009, 2010). This impact was particularly evident between the detaching warm anticyclone and a cold-core cyclone present just to the southeast of this ring where upwelling was enhanced within the cyclone. However, limitations of one-dimensional ocean models may still be significant in less-energetic ocean regions, particularly for relatively slow-moving storms in regions with a relatively thin surface warm layer. The absence of upwelling may significantly reduce the SST cooling in these cases. Furthermore, one-dimensional ocean models predict a purely inertial current response with energy that cannot propagate into the ocean interior through wave dynamics. These factors may be especially important when a storm is closely followed by a second one (e.g., Isidore and Lili in 2002; Katrina and Rita in 2005; Gustav and Ike in 2008).

The urge to design efficient coupled forecast models containing a one-dimensional ocean model is understandable given operational constraints from available computer resources. Although the choice of vertical mixing parameterization has little effect on run time, it was reduced by about 70% in the one-dimensional experiment. Given the results of this study, however, we cannot conclude that a one-dimensional model will always be adequate for performing intensity forecasts. Furthermore, the western boundary regions of ocean basins where the use of three-dimensional ocean models is most likely to be important are located close to land where intensity forecast errors, particularly in regard to rapid intensification and rapid weakening, will have the worst consequences. These questions will ultimately have to be answered by coupled forecast experiments for a large number of storms in different ocean regions and basins.

Existing operational atmospheric models are run at a horizontal resolution that is too coarse to resolve the inner-core TC structure, overestimating R_{MAX} by a factor of 2 and underestimating the maximum wind by 40%–50% in the case of the 27-km COAMPS model. For this reason, the H*WIND wind analysis was blended into fields from the U.S. Navy COAMPS atmospheric model to generate forcing for the control experiment in this study that at least marginally resolved the horizontal scales of the eye and eyewall. An alternate experiment forced by the COAMPS model alone substantially degraded the quality of the simulated ocean response. Research studies of the ocean response to a TC should not use forcing fields from these existing operational atmospheric models. The question of whether the scales resolved by H*WIND are fully adequate could not be addressed here because higher-resolution forcing from an atmospheric model that accurately resolved both the track and intensity of Ivan was not available. Since operational forecast centers are moving toward using nested atmospheric models with resolution of $O(1\ \text{km})$, atmospheric model resolution should not be an issue for coupled TC forecast models in the future.

The accuracy of the upper-ocean thermal response to Ivan was most sensitive to the ocean model initialization. The two important aspects of initialization are ocean feature location and providing accurate profiles of temperature, salinity, and density within the existing features. The control experiment was initialized from a data-assimilative ocean hindcast where the LC, a detaching warm ring, and two associated cold-core cyclones that had a large impact on the final SST cooling pattern were correctly situated. An alternate experiment initialized from a non-assimilative ocean model demonstrated that feature location had a much larger influence on the responses of SST, wind-driven upwelling, and heat flux from the ocean to the atmosphere than did other model and air–sea flux parameterizations. Although this study was conducted in a region where water mass and heat content differences between ocean features was large, large biases in initial temperature, salinity, and density profiles along with the thickness of the warm layer can also significantly degrade upper-ocean SST forecasts in all ocean regions

←

FIG. 12. (top) Taylor diagram comparing the simulated north–south (cross shelf and along track) velocity component from the control experiment to the same field from all of the remaining experiments over the upper 150 m at SEED mooring 9. Symbols and colors follow the conventions used in the top panel of Fig. 8. The large black square represents a perfect comparison. (bottom) Taylor diagram comparing the simulated north–south (cross shelf and along track) velocity component for all experiments to the same field from the ADCP observations at SEED mooring 9. The comparison was performed over the common depth range where both observed and simulated data were available within the upper 150 m of the water column, as shown in Fig. 11. Symbols and colors follow the conventions used in the bottom panel of Fig. 8. The large black square again represents a perfect comparison.

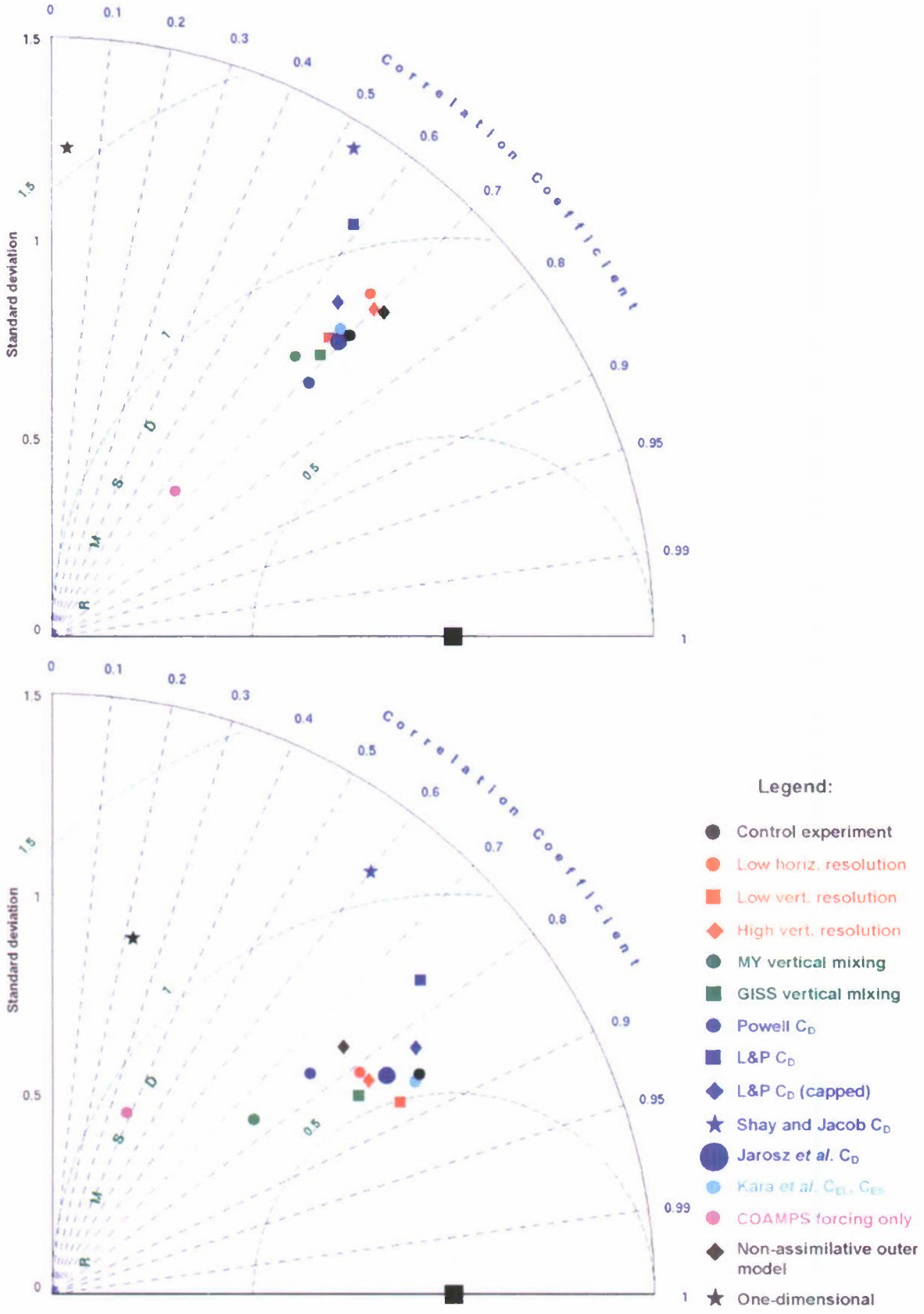
Correlation Coefficient
Standard deviation
0
0.1
0.2
0.3
0.4
0.5
0.6
0.7
0.8
0.9
0.95
0.99
1
1.5
0.5
C
S
M
R
Legend:
Control experiment
Low horiz. resolution
Low vert. resolution
High vert. resolution
MY vertical mixing
GISS vertical mixing
Powell C_D
L&P C_D
L&P C_D (capped)
Shay and Jacob C_D
Jarosz *et al.* C_D
Kara *et al.* C_{EL}, C_{ES}
COAMPS forcing only
Non-assimilative outer model
One-dimensional

TABLE 4. Summary of the impacts of the changes in different model attributes on the SST response pattern, the heat flux from the ocean to the atmosphere, the wind-driven upwelling, and the upper-ocean near-inertial momentum response. Heat flux differences are for the flux averaged over $1.4R_{MAX}$. Sensitivity is measured relative to the control experiment. If the sensitivity depends on the location relative to the energetic ocean features, the impacts on sensitivity are modified by the word "potentially" to indicate that this level of sensitivity may not be true everywhere.

Model attribute	SST response sensitivity [RMS diff from control expt (°C)]	Heat flux sensitivity [diff from control expt (W m^{-2})]	Upwelling sensitivity (diff from control expt)	Upper-ocean momentum sensitivity at SEED 9	Recommendation
Horizontal resolution	Intermediate (0.47°)	Low (<10)	Intermediate (<50 m day^{-1} or <25%)	Low	≈10 km is adequate
Vertical resolution	Low (0.26°–0.29°)	Low (<10)	Low (<10 m day^{-1} or <5%)	Low	≈10 m in the OML is adequate
Vertical mixing	Intermediate (0.37°–0.49°)	High (<250)	High (<120 m day^{-1} or <60%)	Intermediate	KPP is a good choice; MY and GISS give slower cooling, larger heat flux
C_D	High (up to 0.75°)	High (<350)	High (<100 m day^{-1} or <50%)	High (large C_D increases strength and penetration of forced currents)	Donelan, Large and Pond capped, and Jarosz et al. are good choices
C_{EL}, C_{ES}	Low (0.18°)	High (<300)	Low (<20 m day^{-1} or <10%)	Very low	Default COARE 3.0 algorithm in HYCOM is a reasonable choice
Atmospheric forcing	High (0.70°)	High (<250)	High (<140 m day^{-1} or <70%)	Very high	Must resolve inner-core structure (≤10-km resolution)
Outer model	Potentially very high (1.57°)	Potentially very high (<900)	Potentially very high (<160 m day^{-1} or <80%)	Intermediate (potentially very high near energetic ocean features)	Accurate initialization critically important
Ocean dynamics	Potentially very high (1.31°)	Potentially high (<300)	Zero upwelling in 1D experiment	Very high (pure inertial response)	Ocean model must resolve 3D ocean dynamics

(e.g., Ginis 2002). A high priority should therefore be given to improving ocean model initialization.

Air–sea flux parameterizations have an intermediate to high impact on all important aspects of model sensitivity (Table 4). For wind stress, the magnitude of C_D at high wind speeds impacts SST cooling and heat flux from the ocean to the atmosphere by 1) modifying the rate of OML deepening by wind-driven turbulence (friction velocity) and 2) altering the magnitude and three-dimensional structure of wind-driven currents and wind-driven upwelling. For turbulent heat flux, an alternate experiment using a parameterization of C_{EL} and C_{ES} that produced values 20%–40% higher that the one used in the control experiment (Fig. 4) had a large influence on the turbulent heat flux as expected, but had very little impact on SST cooling since entrainment at the OML base makes the dominant contribution to this cooling (e.g., Jacob et al. 2000; Shay and Jacob 2006). Substantial effort will have to be directed toward verifying the parameterizations of the surface flux drag coefficients in coupled TC forecast models.

Although the SST response displayed intermediate sensitivity to the three vertical mixing models tested, both

←

FIG. 13. Taylor diagrams comparing the simulated north–south (cross shelf and along track) velocity component for all experiments to the same field from the ADCP observations at SEED moorings (top) 1 and (bottom) 9. The comparison was performed over the common depth range where both observed and simulated data were available within the upper 150 m of the water column, as shown in Fig. 11. Symbols and colors follow the conventions used in the bottom panel of Fig. 8. The large black square represents a perfect comparison.

wind-driven upwelling and air–sea heat flux displayed high sensitivity that was comparable to the high sensitivity to surface flux drag coefficients. Although a substantial effort to improve the performance of vertical mixing models is warranted, further improvement in model initialization and surface flux parameterizations will first be necessary; otherwise, vertical mixing may be "tuned" to correct for errors and biases resulting from these other factors.

Horizontal resolution has a low to intermediate influence on all important aspects of model performance (Table 4). Although it has intermediate impact on SST cooling, it has only a small influence on the heat flux from the ocean to the atmosphere. This probably results in part because much of the RMS difference occurs at small scales since the higher-resolution experiment provides a sharper resolution of temperature changes across fronts. As a result, these SST differences have only a small impact on area-integrated heat flux. Sensitivity to vertical resolution is low with respect to all important aspects of model performance. Given the greater sensitivity to other model attributes, there is no need to invest a lot of effort into optimizing the model's horizontal or vertical resolution. Based on the Ivan results, ocean models run at a horizontal resolution of $\leq$10 km and a vertical resolution within the OML of $\leq$10 m should be adequate for addressing the greater concerns enumerated above since further increases in resolution will have a small impact on SST cooling and on the heat flux from the ocean to the atmosphere.

Although these results are based on one ocean model for one hurricane in one ocean region, they represent an early step toward designing strategies that will improve the performance of the ocean component of coupled forecast models. Ocean model studies must be extended to other TCs and other ocean regions, while evaluation and sensitivity analysis must also be extended to coupled forecast models. These efforts will require ongoing programs to obtain high quality observations of currents and baroclinic structure with sufficient detail and both three-dimensional and temporal patterns of coverage to perform the detailed evaluation studies required to formulate effective model improvement strategies.

Acknowledgments. This work was sponsored by the National Oceanic and Atmospheric Administration (Grant NA17RJ1226) and the National Science Foundation (Grant ATM0444525). The daily Reynolds blended SST maps were obtained online (http://www.ncdc.noaa.gov/oa/climate/research/sst/description.php). The Office of Naval Research supported the Naval Research Laboratory's basic research project "Slope to Shelf Energetics and Exchange Dynamics" (SEED) under Program Element 0601153N.

REFERENCES

Andreas, E. L, and J. DeCosmo, 2002: The signature of sea spray in the HEXOS turbulent heat flux data. *Bound.-Layer Meteor.*, **103,** 303–333.

Bender, M. A., and I. Ginis, 2000: Real-case simulations of hurricane–ocean interaction using a high-resolution coupled model: Effects on hurricane intensity. *Mon. Wea. Rev.*, **128,** 917–946.

——, ——, R. Tuleya, B. Thomas, and T. Marchok, 2007: The operational GFDL coupled hurricane–ocean prediction system and a summary of its performance. *Mon. Wea. Rev.*, **135,** 3965–3989.

Bleck, R., 2002: An oceanic general circulation framed in hybrid isopycnic–Cartesian coordinates. *Ocean Modell.*, **4,** 55–88.

Canuto, V. M., A. Howard, Y. Cheng, and M. S. Dubovikov, 2001: Ocean turbulence. Part I: One-point closure model—Momentum and heat vertical diffusivities. *J. Phys. Oceanogr.*, **31,** 1413–1426.

——, ——, ——, and ——, 2002: Ocean turbulence. Part II: Vertical diffusivities of momentum, heat, salt, mass, and passive scalars. *J. Phys. Oceanogr.*, **32,** 240–264.

Carnes, M. R., W. J. Teague, and E. Jarosz, 2008: Low-frequency current variability observed at the shelfbreak in the northeastern Gulf of Mexico: November 2004–May 2005. *Cont. Shelf Res.*, **28,** 399–423.

Chassignet, E. P., L. T. Smith, G. R. Halliwell, and R. Bleck, 2003: North Atlantic simulation with the Hybrid Coordinate Ocean Model (HYCOM): Impact of the vertical coordinate choice, reference density, and thermobaricity. *J. Phys. Oceanogr.*, **33,** 2504–2526.

——, H. E. Hurlburt, O. M. Smedstad, G. R. Halliwell, P. J. Hogan, A. J. Wallcraft, and R. Bleck, 2007: The HYCOM (Hybrid Coordinate Ocean Model) data assimilative system. *J. Mar. Syst.*, **65,** 60–83.

Cione, J. J., and E. W. Uhlhorn, 2003: Sea surface temperature variability in hurricanes: Implications with respect to intensity change. *Mon. Wea. Rev.*, **131,** 1783–1795.

Cooper, M., and K. Haines, 1996: Altimetric assimilation with water property conservation. *J. Geophys. Res.*, **101,** 1059–1078.

Cummings, J. A., 2005: Operational multivariate ocean data assimilation. *Quart. J. Roy. Meteor. Soc.*, **131,** 3583–3604.

Donelan, M. A., B. K. Haus, N. Reul, W. J. Plant, M. Stiassnie, H. C. Graber, O. B. Brown, and E. S. Saltzman, 2004: On the limiting aerodynamic roughness of the ocean in very strong winds. *Geophys. Res. Lett.*, **31,** L18306, doi:10.1029/2004GL019460.

Emanuel, K. A., C. DesAutels, C. Holloway, and R. Korty, 2004: Environmental controls of tropical cyclone intensity. *J. Atmos. Sci.*, **61,** 843–858.

Fairall, C. W., E. F. Bradley, J. S. Godfrey, G. A. Wick, J. B. Edson, and G. S. Young, 1996: Cool-skin and warm-layer effects on sea surface temperature. *J. Geophys. Res.*, **101** (C1), 1295–1308.

Ginis, I., 2002: Tropical cyclone–ocean interactions. *Atmosphere–Ocean Interactions*, W. Perrie, Ed., Advances in Fluid Mechanics Series, Vol. 33, WIT Press, 83–114.

Halliwell, G. R., Jr., 2004: Evaluation of vertical coordinate and vertical mixing algorithms in the Hybrid-Coordinate Ocean Model (HYCOM). *Ocean Modell.*, **7,** 285–322.

——, R. H. Weisberg, and D. A. Mayer, 2003: A synthetic float analysis of upper-limb meridional overturning circulation interior ocean pathways in the tropical/subtropical Atlantic. *Interhemispheric Water Exchange in the Atlantic Ocean*, G. Goni and P. Malanotte-Rizzoli, Eds., Elsevier, 93–136.

——, L. K. Shay, S. D. Jacob, O. M. Smedstad, and E. W. Uhlhorn, 2008: Improving ocean model initialization for coupled tropical cyclone forecast models using GODAE nowcasts. *Mon. Wea. Rev.*, **136,** 2576–2591.

——, A. Barth, R. H. Weisberg, P. Hogan, O. M. Smedstad, and J. Cummings, 2009: Impact of GODAE products on nested HYCOM simulations of the West Florida Shelf. *Ocean Dyn.*, **59,** 139–155.

Hodur, R., 1997: The Naval Research Laboratory Coupled Ocean/Atmosphere Mesoscale Prediction System (COAMPS). *Mon. Wea. Rev.*, **125,** 1414–1430.

Hong, X., S. W. Chang, S. Raman, L. K. Shay, and R. Hodur, 2000: The interaction between Hurricane Opal (1995) and a warm core ring in the Gulf of Mexico. *Mon. Wea. Rev.*, **128,** 1347–1365.

Jacob, S. D., and L. K. Shay, 2003: The role of oceanic mesoscale features on the tropical cyclone induced mixed layer response. *J. Phys. Oceanogr.*, **33,** 649–676.

——, ——, A. J. Mariano, and P. G. Black, 2000: The 3D oceanic mixed-layer response to Hurricane Gilbert. *J. Phys. Oceanogr.*, **30,** 1407–1429.

Jaimes, B., and L. K. Shay, 2009: Mixed layer cooling in mesoscale ocean eddies during Hurricanes Katrina and Rita. *Mon. Wea. Rev.*, **137,** 4188–4207.

——, and ——, 2010: Near-inertial wave wake of hurricanes Katrina and Rita over mesoscale oceanic eddies. *J. Phys. Oceanogr.*, **40,** 1320–1337.

Jarosz, E., D. A. Mitchell, D. W. Wang, and W. J. Teague, 2007: Bottom-up determination of air–sea momentum exchange under a major tropical cyclone. *Science*, **315,** 1707–1709.

Kara, A. B., P. A. Rochford, and H. E. Hurlburt, 2002: Air–sea flux estimates and the 1997–1998 ENSO event. *Bound.-Layer Meteor.*, **103,** 439–458.

Large, W. G., and S. Pond, 1981: Open ocean momentum flux measurements in moderate to strong winds. *J. Phys. Oceanogr.*, **11,** 324–336.

——, J. C. McWilliams, and S. C. Doney, 1994: Oceanic vertical mixing: A review and a model with a nonlocal boundary layer parameterization. *Rev. Geophys.*, **32,** 363–403.

Leipper, D. F., and D. Volgenau, 1972: Hurricane heat potential of the Gulf of Mexico. *J. Phys. Oceanogr.*, **2,** 218–224.

Lin, I.-I., C.-C. Wu, K. A. Emanuel, I.-H. Lee, C.-R. Wu, and I.-F. Pun, 2005: The interaction of Supertyphoon Maemi (2003) with a warm ocean eddy. *Mon. Wea. Rev.*, **133,** 2635–2649.

——, ——, and I.-F. Pun, 2008: Upper ocean thermal structure and the western North Pacific category 5 typhoons. Part I: Ocean features and the category 5 typhoons' intensification. *Mon. Wea. Rev.*, **136,** 3288–3306.

Mainelli, M., M. DeMaria, L. K. Shay, and G. Goni, 2008: Application of oceanic heat content estimation to operational forecasting of recent category 5 hurricanes. *Wea. Forecasting*, **23,** 3–16.

Mellor, G. L., and T. Yamada, 1982: Development of a turbulence closure model for geophysical fluid problems. *Rev. Geophys. Space Phys.*, **20,** 851–875.

Murphy, A. H., 1988: Skill scores based on the mean square error and their relationships to the correlation coefficient. *Mon. Wea. Rev.*, **116,** 2417–2424.

Powell, M. D., S. H. Houston, L. R. Amat, and N. Morisseau-Leroy, 1998: The HRD real-time hurricane wind analysis system. *J. Wind Eng. Ind. Aerodyn.*, **78,** 53–64.

——, P. J. Vickery, and T. A. Reinhold, 2003: Reduced drag coefficient for high wind speeds in tropical cyclones. *Nature*, **422,** 279–283.

Price, J. F., 1981: Upper ocean response to a hurricane. *J. Phys. Oceanogr.*, **11,** 153–175.

Reynolds, R. W., T. M. Smith, C. Liu, D. B. Chelton, K. S. Casey, and M. G. Schlax, 2007: Daily high-resolution blended analyses for sea surface temperature. *J. Climate*, **20,** 5473–5496.

Sanford, T. B., J. F. Price, J. B. Girton, and D. C. Webb, 2007: Highly resolved ocean response to a hurricane. *Geophys. Res. Lett.*, **34,** L13604, doi:10.1029/2007GL029679.

Schade, L. R., and K. A. Emanuel, 1999: The ocean's effect on the intensity of tropical cyclones: Results from a simple coupled atmosphere–ocean model. *J. Atmos. Sci.*, **56,** 642–651.

Scharroo, R., W. H. Smith, and J. L. Lillibridge, 2005: Satellite altimetry and the intensification of Hurricane Katrina. *Eos, Trans. Amer. Geophys. Union*, **86,** 366–367.

Shay, L. K., 2009: Upper ocean structure: Response to strong forcing events. *Encyclopedia of Ocean Sciences*, 2nd ed. J. Steele et al., Eds., Elsevier, 4619–4637.

——, and R. L. Elsberry, 1987: Near-inertial ocean current response to Hurricane Frederic. *J. Phys. Oceanogr.*, **17,** 1249–1269.

——, and S. D. Jacob, 2006: Relationship between oceanic energy fluxes and surface winds during tropical cyclone passage. *Advances in Fluid Mechanics*, W. Perrie, Ed., *Atmosphere–Ocean Interactions II*, WIT Press, 115–142.

——, and E. W. Uhlhorn, 2008: Loop Current response to Hurricanes Isidore and Lili. *Mon. Wea. Rev.*, **136,** 3248–3274.

——, R. L. Elsberry, and P. G. Black, 1989: Vertical structure of the ocean current response to a hurricane. *J. Phys. Oceanogr.*, **19,** 1249–1269.

——, G. J. Goni, and P. G. Black, 2000: Effects of a warm oceanic feature on Hurricane Opal. *Mon. Wea. Rev.*, **128,** 1366–1383.

Shen, W., I. Ginis, and R. E. Tuleya, 2002: A numerical investigation of land surface water on landfalling hurricanes. *J. Atmos. Sci.*, **59,** 789–802.

Sun, D., R. Gautam, G. Cervone, Z. Boyeyi, and M. Kaptos, 2006: Comments on satellite altimetry and the intensification of hurricane Katrina. *Eos, Trans. Amer. Geophys. Union*, **87** (8), 89.

Taylor, K. E., 2001: Summarizing multiple aspects of model performance in a single diagram. *J. Geophys. Res.*, **106,** 7183–7192.

Teague, W. J., E. Jarosz, M. R. Carnes, D. A. Mitchell, and P. J. Hogan, 2006: Low-frequency current variability observed at the shelfbreak in the northeastern Gulf of Mexico: May–October 2004. *Cont. Shelf Res.*, **26,** 2559–2582.

——, ——, D. W. Wang, and D. A. Mitchell, 2007: Observed oceanic response over the upper continental slope and outer shelf during Hurricane Ivan. *J. Phys. Oceanogr.*, **37,** 2181–2206.

Wada, A., and N. Usui, 2007: Importance of tropical cyclone heat potential for tropical cyclone intensity and intensification in the western North Pacific. *J. Oceanogr.*, **63,** 427–447.

Walker, N., R. R. Leben, and S. Balasubramanian, 2005: Hurricane forced upwelling and chlorophyll a enhancement within cold core cyclones in the Gulf of Mexico. *Geophys. Res. Lett.*, **32,** L18610, doi:10.1029/2005GL023716.

Wu, C.-C., C.-Y. Lee, and I.-I. Lin, 2007: The effect of the ocean eddy on tropical cyclone intensity. *J. Atmos. Sci.*, **64,** 3562–3578.

Wu, L., B. Wang, and S. A. Braun, 2005: Impacts of air–sea interaction on tropical cyclone track and intensity. *Mon. Wea. Rev.*, **133,** 3299–3314.